JCB Journal of Cell Biology

ARTICLE

TMBIM-2 orchestrates systemic mitochondrial stress response via facilitating Ca^{2+} oscillations

Jiasheng Li[1,2], Jimeng Cui[1,2], Xinyu Li[1,2], Di Zhu[1,2], Zhenhua Chen[1,2], Xiahe Huang[1], Yingchun Wang[1,2], Qingfeng Wu[1,2], and Ye Tian[1,2]

Neuronal mitochondrial function is critical for orchestrating inter-tissue communication essential for overall fitness. Despite its significance, the molecular mechanism underlying the impact of prolonged mitochondrial stresses on neuronal activity and how they orchestrate metabolism and aging remains elusive. Here, we identified the evolutionarily conserved transmembrane protein XBX-6/TMBIM-2 as a key mediator in the neuronal-to-intestinal mitochondrial unfolded protein response (UPR^{mt}). Our investigations reveal that intrinsic neuronal mitochondrial stress triggers spatiotemporal Ca^{2+} oscillations in a TMBIM-2-dependent manner through the Ca^{2+} efflux pump MCA-3. Notably, persistent Ca^{2+} oscillations at synapses of ADF neurons are critical for facilitating serotonin release and the subsequent activation of the neuronal-to-intestinal UPR^{mt}. TMBIM2 expression diminishes with age; however, its overexpression counteracts the age-related decline in aversive learning behavior and extends the lifespan of *Caenorhabditis elegans*. These findings underscore the intricate integration of chronic neuronal mitochondrial stress into neurotransmission processes via TMBIM-2-dependent Ca^{2+} equilibrium, driving metabolic adaptation and behavioral changes for the regulation of aging.

Introduction

The nervous system plays a pivotal role in orchestrating organism-wide adaptations, enabling effective responses to local stress stimuli and ultimately enhancing overall fitness (Carter, 2019; Li and Sheng, 2022; Monzel et al., 2023; Südhof, 2018; van der Kolk, 2006). As non-mitotic and long-lived cells, neurons are exceptionally susceptible to proteotoxic challenges and metabolic stresses that become more pronounced with aging (Devine and Kittler, 2018; Labbadia and Morimoto, 2015). These age-related disturbances in neuronal mitochondrial function have far-reaching effects beyond the neurons themselves. Such disruptions can exert effects on the metabolic status of peripheral tissues and may lead to behavioral modifications (Bar-Ziv et al., 2020). Notably, the accumulation of toxic and aggregated proteins within neurons often coincides with metabolic abnormalities in peripheral tissues, a phenomenon frequently observed in the context of neurodegenerative diseases (Cai et al., 2012; Duarte et al., 2013).

Extensive studies in *Caenorhabditis elegans* have demonstrated that neuronal mitochondrial stress can trigger non-autonomous effects in peripheral tissues. This includes the activation of the mitochondrial unfolded protein response (UPR^{mt}) within the intestine, facilitated by secreted factors like the morphogen Wnt/EGL-20, TGF-β, a variety of neuropeptides, and neurotransmitters such as serotonin (Berendzen et al., 2016; Chen et al., 2021; Shao et al., 2016; Wang et al., 2024; Zhang et al., 2018). The UPR^{mt} is a transcriptional response that orchestrates the upregulation of genes involved in maintaining mitochondrial quality control and metabolic adaptations, ultimately restoring mitochondrial proteostasis (Anderson and Haynes, 2020; Shpilka and Haynes, 2018; Zhu et al., 2022). Various perturbations in neuronal mitochondria, such as diminished mitochondrial electron transport chain (ETC) activity, disruptions in mitochondrial dynamics, and disturbances in mitochondrial proteostasis, have all been linked to cell non-autonomous UPR^{mt} activation (Berendzen et al., 2016; Chen et al., 2021; Durieux et al., 2011; Li et al., 2023; Liu et al., 2022; Shao et al., 2016; Zhang et al., 2021b; Zhang et al., 2018). These findings collectively emphasize the significant role played by neuronal mitochondrial stress in orchestrating systemic stress adaptation in the organism.

The indispensability of mitochondria in the homeostatic regulation of neurons is evident, with their multifaceted role encompassing the generation of ATP and calcium buffering capacity crucial for presynaptic release properties (Gherardi et al., 2020). Mitochondrial calcium, in particular, not only enhances mitochondrial activity but also promotes the functionality of

[1]State Key Laboratory of Molecular Developmental Biology, Institute of Genetics and Developmental Biology, Chinese Academy of Sciences, Beijing, China; [2]University of Chinese Academy of Sciences, Beijing, China.

Correspondence to Ye Tian: ytian@genetics.ac.cn.

https://doi.org/10.1083/jcb.202408050

mitochondrial enzymes (Gherardi et al., 2020). An excessive accumulation of Ca^{2+} within mitochondria can directly disrupt mitochondrial function and potentially trigger apoptosis (Berridge et al., 2003; Giorgi et al., 2018; Orrenius et al., 2003). Despite this understanding, the intricate molecular mechanism governing how enduring chronic mitochondrial stress modulates neurotransmission, effectively coordinating systemic stress communication, and influencing the aging process, remains largely unknown.

To investigate how organisms coordinate systemic stress responses in the face of persistent neuronal mitochondrial perturbations, we conducted a genetic screening in *C. elegans* to identify factors involved in the activation of neuronal-to-intestinal UPR^{mt}. Our screening identified a mutant, *xbx-6*, which exhibited a strong suppression of UPR^{mt}. The *xbx-6* encodes a transmembrane protein belonging to the evolutionarily conserved transmembrane Bax-inhibiting domain (TMBIM) family, showing homology to TMBIM2. Intriguingly, we observed a striking phenomenon: perturbations in neuronal mitochondria led to the generation of Ca^{2+} oscillations that persisted for several days in vivo. This process is dependent on the presence of *xbx-6/tmbim-2*. Our findings uncovered that TMBIM-2 couples with a Ca^{2+} pump, MCA-3 (known as PMCA in mammals), to re-establish low Ca^{2+} levels after spikes induced by mitochondrial stress. The enduring Ca^{2+} fluctuations observed at synapses of ADF neurons play a pivotal role in facilitating serotonin release, which is crucial for activating the neuronal-to-intestinal UPR^{mt} under conditions of persistent neuronal mitochondrial stress. Additionally, our analysis of existing datasets revealed a consistent trend: the expression of TMBIM2 in neurons decreases with age across diverse species, including *C. elegans*, mice, and humans. Notably, overexpression of TMBIM-2 in *C. elegans* neurons not only mitigates age-related cognitive decline but also extends lifespan. In summary, our study provides insights into the intricate network of interactions governing the response of neurotransmission to chronic neuronal mitochondrial stresses via Ca^{2+} signaling.

Results

XBX-6/TMBIM-2 functions in neurons to coordinate neuronal-to-intestinal UPR^{mt} activation

To investigate the intricate mechanism governing the coordination of neuronal-to-intestinal mitochondrial stress communication and its consequential impact on systemic metabolic changes, we initiated a genetic suppressor screen. We aimed to identify mutants displaying impaired communication of the UPR^{mt} signal from neurons to the intestine. We focused on the neuronal expression of a Wnt ligand, EGL-20, driven by the pan-neuron promoter *rgef-1*, as evidenced by its impact on the induction of the UPR^{mt} reporter DVE-1::GFP in the intestine of *C. elegans* (Li et al., 2022; Zhang et al., 2018).

We screened ~3,400 mutagenized genomes, identifying 42 mutants that exhibited compromised activation of intestinal UPR^{mt} upon neuronal expression of Wnt/EGL-20. Among these mutants, *yth57* stood out due to its robust suppression of neuronal-to-intestinal UPR^{mt} activation but did not exhibit a similar inhibitory effect on UPR^{mt} activation driven by intestinal Wnt/EGL-20 overexpression under the control of intestinal (*gly-19*) promoters (Fig. 1, A and B). This unique phenotype directed us to further characterize the *yth57* mutant. Whole-genome sequencing revealed that *yth57* carries a G to A nucleotide mutation in the *xbx-6* gene, leading to the amino acid substitution Val275Ile (Fig. 1 C). *xbx-6* encodes a transmembrane protein that belongs to the evolutionarily conserved transmembrane BAX inhibitor motif-containing (TMBIM) proteins. Notably, the homology between XBX-6 and the human TMBIM2 prompted us to generate transgenic worms expressing hTMBIM2 (Fig. S1 A). The alpha fold result showed that the C segment of TMBIM-2 contained seven transmembrane regions (Fig. S1, B and C). Expression of hTMBIM2 partially restored intestinal UPR^{mt} activation in *tmbim-2(yth57)* mutants with neuronal Wnt/EGL-20 expression, indicating a high degree of conservation in the function of TMBIM2 (Fig. S1, D and E). Thus, we designated *xbx-6* as *tmbim-2*, facilitating a clearer connection between our findings and its human counterpart (Liu, 2017; Rojas-Rivera and Hetz, 2015; Zhang et al., 2018).

To determine the involvement of TMBIM-2 in cell non-autonomous activation of UPR^{mt} triggered by various forms of neuronal mitochondrial perturbations, we employed CRISPR/Cas9 gene editing to generate distinct alleles of *tmbim-2* deletion mutants, namely *yth26* and *yth130*, across different genetic backgrounds (Fig. 1 C). The absence of *tmbim-2* strongly suppressed the intestinal UPR^{mt} activation in response to either neuronal Q40::YFP expression or neuronal knockdown (KD) of cytochrome oxidase assembly protein (*cox-5B/cco-1*) by expressing *cox-5B* hairpin (HP) under *unc-119* promoter (Fig. 1, D–G and Fig. S1, F–M). In contrast, *tmbim-2* mutants did not impact cell-autonomous intestinal UPR^{mt} activation caused by *cox-5B* RNAi (Fig. 1, D and E; and Fig. S1, F and G).

To determine whether TMBIM-2's role in cell non-autonomous UPR^{mt} activation is linked to its neuronal expression, we expressed *tmbim-2* under tissue-specific promoters in a *tmbim-2* mutant background. Expression of *tmbim-2* driven by the pan-neuron promoter *rgef-1p* or the ciliated sensory neuron promoter *xbx-1p* effectively rescued the suppressed intestinal UPR^{mt} activation in *tmbim-2* mutants with either neuronal Wnt/EGL-20 expression or neuronal Q40::YFP expression (Fig. 1, F and G; and Fig. S1, N–P). Furthermore, restoring suppressed intestinal UPR^{mt} activation in *tmbim-2* mutants was also achieved by expressing *tmbim-2* exclusively in two amphid sensory ADF neurons but not in NSM or other sensory neurons (Fig. 1, H and I). In contrast, the expression of *tmbim-2* driven by *gly-19* promoters failed to restore the intestinal UPR^{mt} activation in *tmbim-2(yth57)* mutants with neuronal Wnt/EGL-20 or Q40::YFP expression (Fig. 1, F and G; and Fig. S1, N–P). Additionally, CRISPR/Cas9-mediated knockout of *tmbim-2* in ADF neurons robustly suppressed the intestinal activation of UPR^{mt} in response to neuronal Q40::YFP expression (Fig. S1, Q and R). These results indicate a critical function of *tmbim-2* within ADF neurons in orchestrating intestinal activation of UPR^{mt} in response to neuronal mitochondrial perturbations.

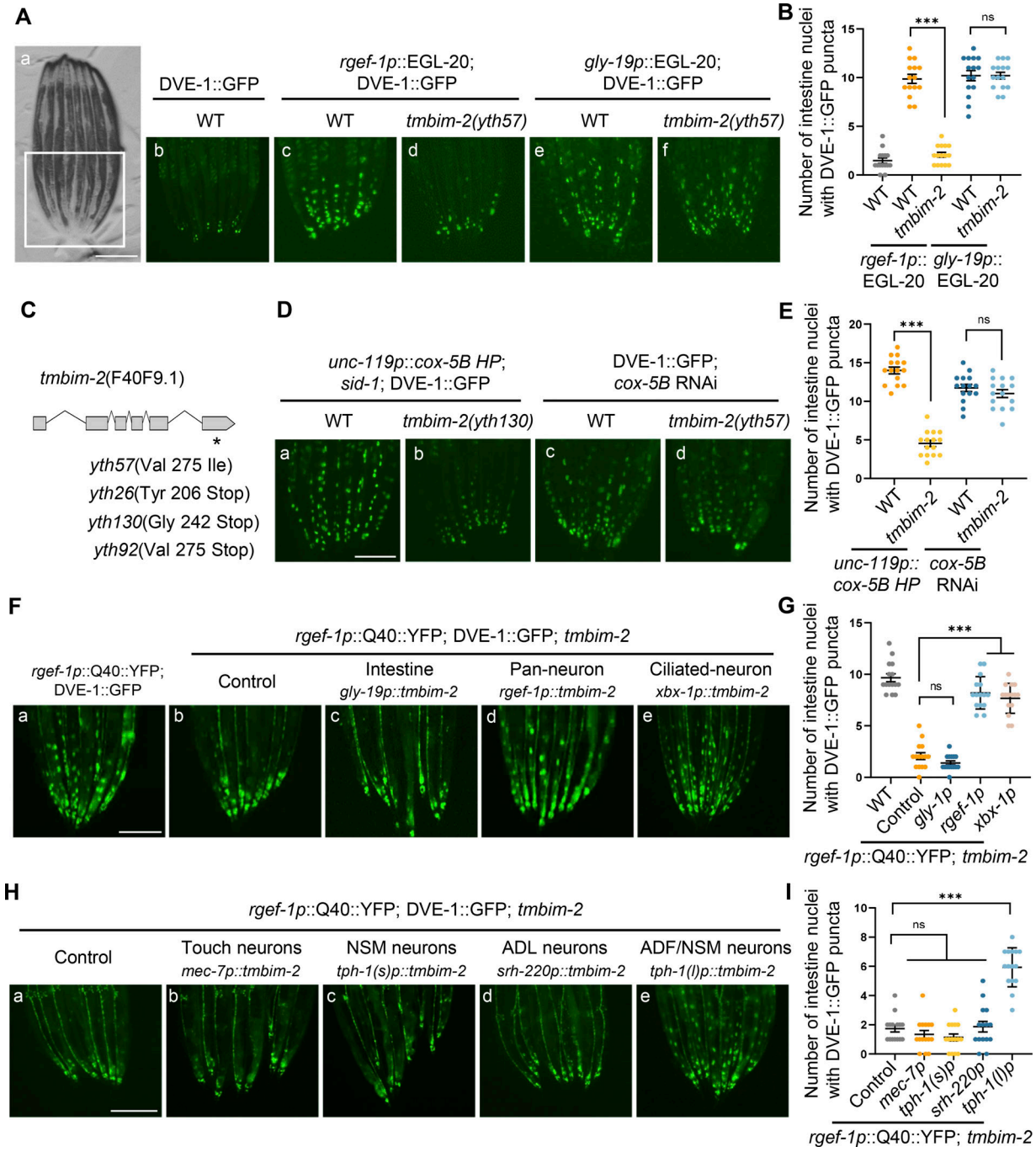

Figure 1. **XBX-6/TMBIM-2 deficiency suppressed the neuronal-to-intestinal UPR^{mt} activation. (A)** Representative photomicrographs demonstrating: bright-field images of aligned, wild-type (WT) animals. The area shown in white box is the region for imaging in Fig. 1 **(a)**; the expression pattern of the *dve-1(zcIs39[dve-1p::dve-1::gfp])* reporter in WT day 2 adult animals **(b)**; *dve-1* reporter expression in neuronal EGL-20 *(ythIs3[rgef-1p::egl-20 + myo-2p::tdtomato])* animals **(c)**; neuronal EGL-20; *tmbim-2(yth57)* animals **(d)**; intestinal EGL-20 *(ythIs1[gly-19p::egl-20])* animals **(e)**; intestinal EGL-20; *tmbim-2(yth57)* animals **(f)**, respectively. The posterior region of the intestine where DVE-1::GFP is induced or suppressed is highlighted. **(B)** Quantification of the number of intestinal nuclei puncta with GFP signal per worm as shown in A. **(C)** A schematic diagram of three mutant alleles *yth26*, *yth57*, and *yth130* of *tmbim-2*. **(D)** Representative photomicrographs demonstrating: *dve-1* reporter expression in neuronal *cox-5B* knockdown *(uthIs375[unc-119p::cox-5B HP; pRF(rol-6)]); sid-1(qt9)* animals **(a)**; neuronal *cox-5B* knockdown; *sid-1(qt9); tmbim-2(yth130)* animals **(b)**; WT animals **(c)**; and *tmbim-2 (yth57)* **(d)** grown on *cox-5B* RNAi from hatching. The posterior region of the intestine where DVE-1::GFP is induced or suppressed is highlighted. **(E)** Quantification of the number of intestinal nuclei puncta with GFP signal per worm as shown in D. **(F)** Representative photomicrographs demonstrating: the expression pattern of *dve-1* reporter in WT animals expressing neuronal Q40 *(rmIs110[rgef-1p::Q40::YFP]* **(a)**; *dve-1* reporter expression in *tmbim-2 (yth57)* animals expressing neuronal Q40 **(b)**; intestinal rescue TMBIM-2 *(ythEx289[gly-19p::tmbim-2])* **(c)**; pan-neuronal rescue TMBIM-2 *(ythEx290[rgef-1p::tmbim-2])* **(d)**; ciliated-neuronal rescue TMBIM-2 *(ythEx476[xbx-1p::tmbim-2])* **(e)**. The posterior region of the intestine where DVE-1::GFP is induced or suppressed is highlighted. **(G)** Quantification of the number of intestinal nuclei puncta with GFP signal per worm as shown in F. **(H)** Representative photomicrographs demonstrating: *dve-1* reporter expression in *tmbim-2 (yth57)* animals expressing neuronal Q40::YFP **(a)**; touch neurons rescue TMBIM-2 *(ythEx568[mec-7p::tmbim-2])* **(b)**; NSM neurons rescue TMBIM-2 *(ythEx772[tph-1(s)p::tmbim-2])* **(c)**; ADL neurons

rescue TMBIM-2 (*ythEx569[srh-220p::tmbim-2]*) **(d)**; ADF/NSM neurons rescue TMBIM-2 (*ythEx773[tph-1(l)p::tmbim-2]*) **(e)**. The posterior region of the intestine where DVE-1::GFP is induced or suppressed is highlighted. **(I)** Quantification of the number of intestinal nuclei puncta with GFP signal per worm as shown in H. ***P < 0.001, ns denotes P > 0.05 via unpaired two-tailed Student's *t* test. Error bars, SEM. $n \geq 15$ worms. Scale bar, 250 µm.

The expression and subcellular distribution of TMBIM-2 in response to neuronal mitochondrial stress

The TMBIM gene family, distinguished by seven transmembrane domains, exhibits diverse intracellular membrane localizations, including the plasma membrane, endoplasmic reticulum, and mitochondria, revealing its versatile presence across cellular compartments (Rojas-Rivera and Hetz, 2015). To investigate the subcellular localization of TMBIM-2, we employed transgenic animals expressing *tmbim-2* fused with GFP under its native promoter. The functionality of TMBIM-2::GFP was validated through its ability to restore intestinal UPR^{mt} activation in *tmbim-2(yth57)* mutants (Fig. S2, A and B). Our analysis revealed predominant expression of TMBIM-2::GFP within the nervous system, as indicated by the pan-neuronal *rgef-1p::mCherry* reporter, consistent with recent single-cell RNAseq analysis in *C. elegans* (Roux et al., 2023) (Fig. S2, C and D). In addition to the nervous system, we also observed TMBIM-2 expression in spermatheca and hypodermis (Fig. S2 C).

Notably, we observed an induction of *tmbim-2* expression in response to neuronal mitochondrial stress, highlighting its dynamic regulation (Fig. 2, A–C). Next, we focused on the subcellular distribution of TMBIM-2 and noted its presence in the plasma membrane of neurons (Fig. 2 D). This plasma membrane localization was further validated through co-localization studied with DiD, a lipophilic dye marking the plasma membrane of ciliated sensory neurons (Fig. 2 D). We also confirmed that the localization of TMBIM-2::GFP is excluded from mitochondria in neurons (Fig. S2 E). Furthermore, we detected the presence of TMBIM-2::GFP throughout axons, with a pronounced enrichment at synapses, as evidenced by utilizing presynaptic reporter strain Scarlet::RAB-3 and mCherry::SYD-1 (Fig. 2 E and Fig. S2 F). Notably, under conditions of neuronal mitochondrial stresses, the expression of TMBIM-2 becomes pronounced in the region proximal to the plasma membrane and synapses (Fig. 2 F). To investigate the subcellular localization of TMBIM-2, we performed colocalization experiments. The results revealed that TMBIM-2 partially localizes to the Golgi apparatus (Fig. S2, G and H). These observations collectively suggest that disruptions in neuronal mitochondrial function result in the accumulation of TMBIM-2 along both the plasma membrane and synaptic sites.

Neuronal mitochondrial perturbation triggers spatiotemporal dynamics of Ca^{2+} oscillations in a TMBIM-2-dependent manner

Given the predicted role of TMBIM family proteins in maintaining Ca^{2+} equilibrium within various compartmentalized organelles (Liu, 2017), we hypothesized that TMBIM-2 might play a crucial role in orchestrating the delicate balance of Ca^{2+} within the synapse of ADF neurons, thereby contributing to intricate stress signaling coordination. To test this hypothesis, we generated transgenic *C. elegans* lines expressing the well-established genetically encoded calcium indicator GCaMP6f (Chen et al., 2013; Zhang et al., 2021a). By utilizing the *xbx-1* promoter, we controlled the expression of various forms of GCaMP6f: a plasma membrane–targeted variant (PM-GCaMP6f) (Zhou et al., 2017), a cytosolic-targeted version (cyto-GCaMP6f) (Zhang et al., 2021a), and a mitochondria-targeted form (Mito-GCaMP6f) (Shen et al., 2014). Simultaneously, we employed the ADF neuron-specific *srh-142* promoter to drive Scarlet::RAB-3 expression for labeling the synapses of ADF neurons. This approach enabled visualization of Ca^{2+} flux within distinct subcellular compartments within the synapse of ADF neurons (Fig. 3 A; and Fig. S3, A and B) (Shen et al., 2014; Zhang et al., 2021a).

We initially assessed the localization accuracy of PM-GCaMP6f and Mito-GCaMP6f through colocalization studies with corresponding compartmentalized markers. Our findings revealed that PM-GCaMP6f colocalized with the plasma membrane marker DiD, confirming its plasma membrane localization (Fig. S3 C). Furthermore, Mito-GCaMP6f was found to be enclosed by validated mitochondrial outer membrane reporters, confirming its mitochondrial localization (Fig. S3 D). Subsequently, we investigated the response of these GCaMP6f variants to specific genetic perturbations. We observed an increase in PM-GCaMP6f expression in *egl-19(ad695 gf)* mutants, a voltage-gated calcium channel (Fig. S3, E and F), while Mito-GCaMP6f levels significantly decreased in *mcu-1(ju1154)* mutants, a mitochondrial calcium uniporter (MCU; Fig. S3, G and H). These results indicate that GCaMP6f accurately localizes to subcellular compartments and serves as a reliable indicator of Ca^{2+} dynamics.

When monitoring the plasma membrane-tethered PM-GCaMP6f, worms with neuronal *cox-5B* KD exhibited substantial increases in both the amplitude and frequency of Ca^{2+} waves at synapses of ADF neurons (Fig. 3, B–E and Video 1). Subsequently, we observed a significant decrease in mitochondrial Ca^{2+} waves at synapses of ADF neurons in neuronal *cox-5B* KD worms compared with control animals, as monitored by Mito-GCaMP6f, consistent with the notion that mitochondrial function is disrupted in these animals (Fig. 3, F–I). Surprisingly, in contrast to the distinct dynamics observed with PM-GCaMP6f and Mito-GCaMP6f, we did not observe discernible differences in cytosolic GCaMP6f dynamics between control and neuronal *cox-5B* KD worms (Fig. 3, J–L), suggesting that the mild disruption of neuronal mitochondrial function did not substantially impact the overall cytosolic Ca^{2+} balance. One plausible explanation for this phenomenon is that calcium pumps swiftly export locally increased Ca^{2+} levels during mitochondrial stresses, thereby not changing the overall cytosolic Ca^{2+} balance. Additionally, the amplitude of Ca^{2+} oscillations in response to chronic neuronal mitochondrial stresses exhibited a gradual increase as worms grew, reaching their peak during young

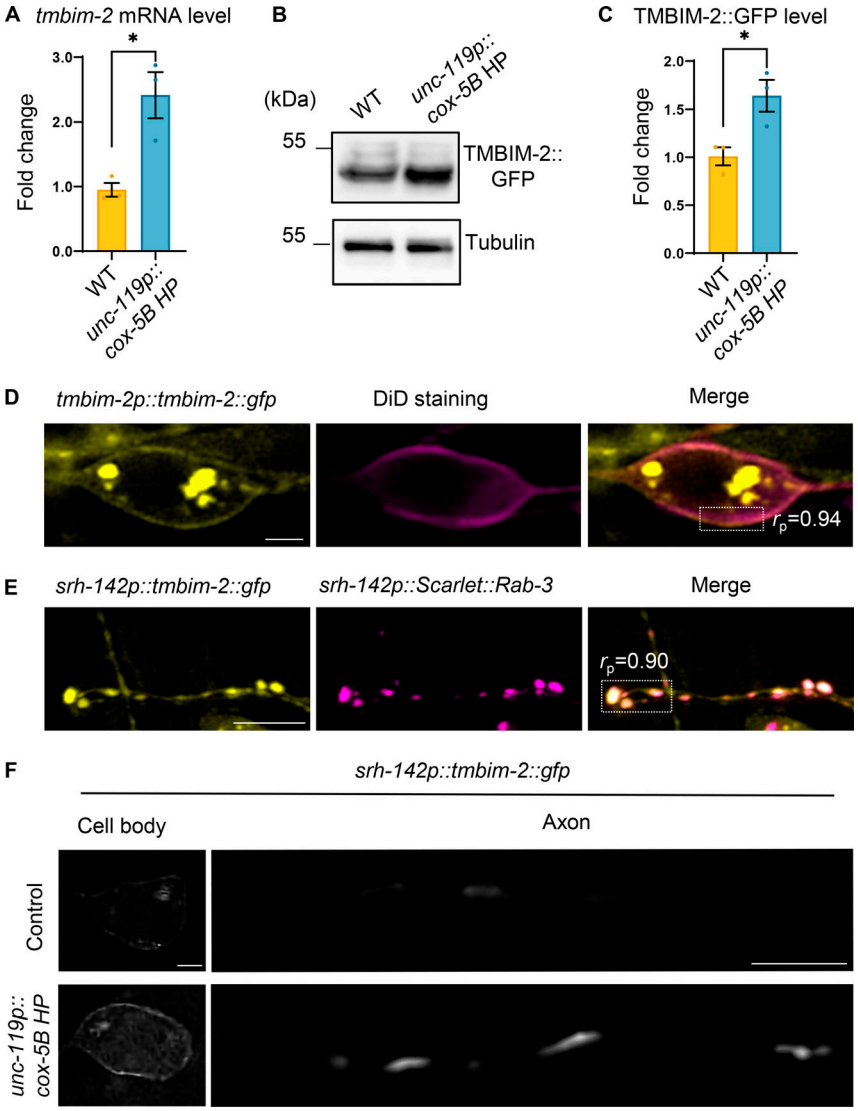

Figure 2. **The expression and subcellular distribution of TMBIM-2 in response to neuronal mitochondrial stress. (A)** Quantification of *tmbim-2* mRNA levels in young adult WT (yellow) and neuronal *cox-5B* knockdown *(uthIs375[unc-119p::cox-5B HP; pRF(rol-6)])* (blue) animals. $n \geq 3$ biologically independent samples. **(B)** Immunoblot of young adult TMBIM-2::GFP expression in WT and neuronal *cox-5B* knockdown animals. **(C)** Quantification of TMBIM-2::GFP protein levels as shown in B: WT (yellow) and neuronal *cox-5B* knockdown (blue) animals; $n \geq 3$ biologically independent samples. **(D)** Representative confocal photomicrographs of day 1 adult animals with *ythEx572 [tmbim-2p::tmbim-2::gfp]* in combination with a lipophilic plasma membrane dye DiD at the cell body. The imaging used Z-planes. Scale bar, 2 µm. Pearson's correlation coefficient (r) for the ROI is 0.94. **(E)** Representative confocal photomicrographs of day 1 adult animals with TMBIM-2 in combination with an ADF synaptic vesicle marker *ythEx536 [srh-142p::tmbim-2::gfp+srh-142p::Scarlet::rab-3]*. The imaging used Z-stacks. Scale bar, 5 µm. Pearson's correlation coefficient (r) for the ROI is 0.90. **(F)** Representative Single Slice-SIM photomicrographs of ADF neuron overexpressing TMBIM-2 *(ythIs102[srh-142p::tmbim-2::gfp])* animals with the presence or absence of neuronal *cox-5B* knockdown. The imaging used Z-planes. Scale bar, 10 µm. *P < 0.05 via unpaired two-tailed Student's *t* test. Error bars, SEM. Source data are available for this figure: SourceData F2.

adulthood and Day 1, followed by a gradual decline with aging (Fig. 7 F). This pattern suggests that the ability of neurons to maintain Ca^{2+} homeostasis in response to chronic mitochondrial stresses declines with age.

Remarkably, the absence of *tmbim-2* resulted in a significant reduction in both the amplitude and frequency of Ca^{2+} waves near the plasma membrane within the synapse of ADF neurons triggered by neuronal *cox-5B* KD, as monitored by PM-GCaMP6f (Fig. 3, B–E). However, the absence of *tmbim-2* did not impact mitochondrial Ca^{2+} waves within the synapse of ADF neurons in neuronal *cox-5B* KD worms (Fig. 3, F–I). To investigate the regulation of Ca^{2+} homeostasis by TMBIM-2, we assessed fluorescence minimum (F_{min}) levels in ADF neurons of *tmbim-2* mutants. Our findings revealed that *tmbim-2* mutant worms exhibited significantly higher F_{min} Ca^{2+} levels in neuronal *cox-5B* KD animals compared with WT control worms (Fig. S3 I). Additionally, mitochondrial Ca^{2+} levels remained unchanged in *tmbim-2* mutant worms (Fig. S3 J). Overexpression of TMBIM-2 within ADF neurons did not significantly change plasma membrane Ca^{2+} waves within the synapse of ADF neurons (Fig. S3, K and L). These collective findings suggest that chronic perturbations in neuronal mitochondria trigger dynamic Ca^{2+} waves in proximity to the plasma membrane in a manner dependent on *tmbim-2*.

Loss of *mcu-1* triggers plasma-membrane Ca^{2+} oscillations within synapses of ADF neurons and activates intestinal UPR^{mt}

Mitochondrial perturbations that decrease mitochondrial membrane potential can lead to decreased ATP production and reduced mitochondrial calcium buffering capacity, thereby altering calcium dynamics near the plasma membrane within neurons (Giacomello et al., 2020). Calcium uptake by mitochondria is facilitated by the MCU, a highly selective and conductive calcium channel encoded by *mcu-1* gene in *C. elegans* (Cao et al., 2017; Doser et al., 2024; Phillips et al., 2019). MCU-1 plays a critical role in calcium homeostasis, enabling dendritic mitochondria to uptake calcium (Ca^{2+}), which in turn promotes the upregulation of mitoROS production. Moreover, mitochondria are positioned in close

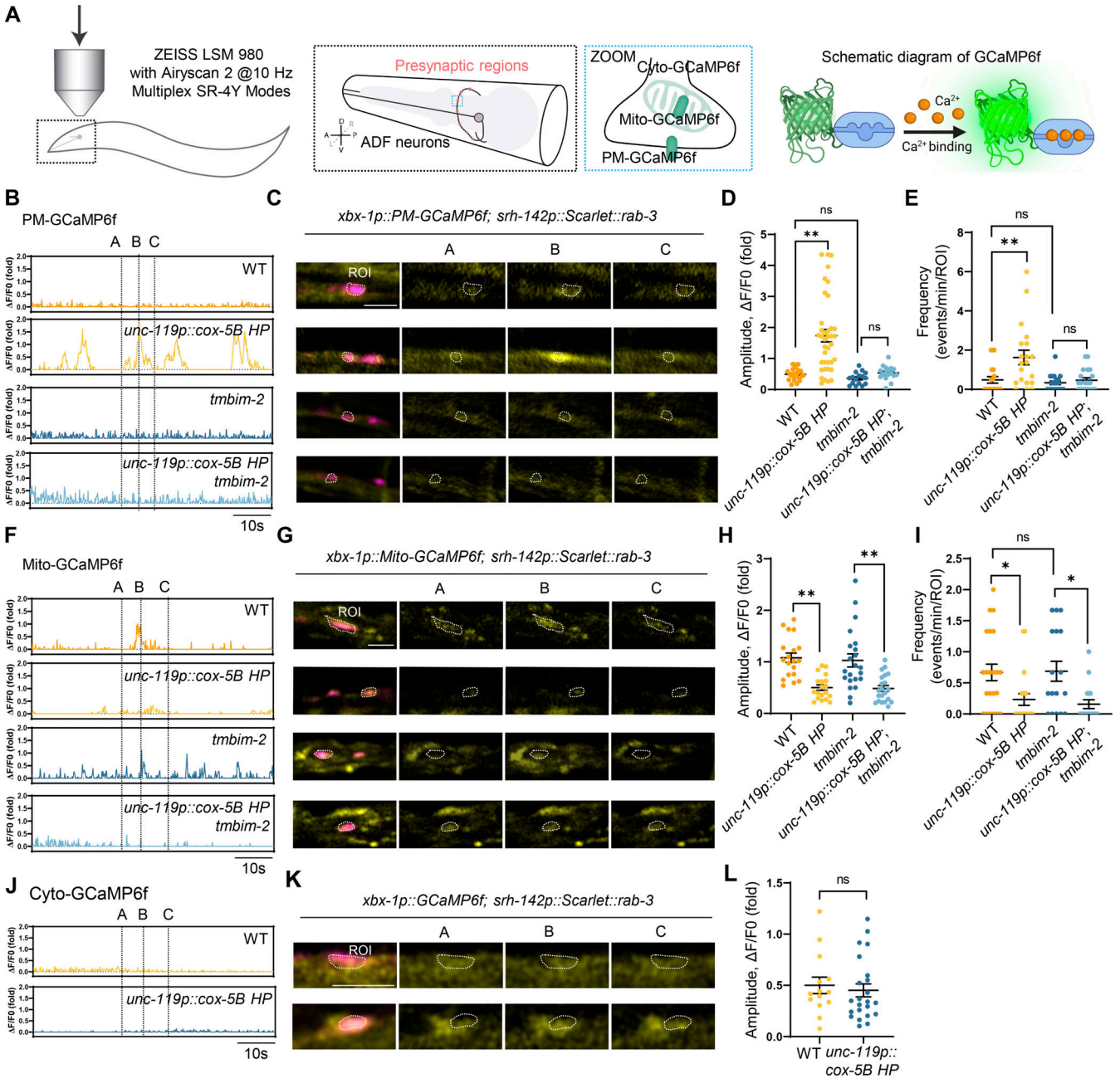

Figure 3. **Neuronal mitochondrial perturbation triggers spatiotemporal dynamics of Ca^{2+} waves in ADF synapses in a TMBIM-2-dependent manner.** **(A)** Schematic drawing of ADF neurons and GCaMP6f imaging regions in B–L, and representation illustrating the principle behind the GCaMP6f. **(B)** Representative fluorescence traces of average background-subtracted fluorescence intensity $\Delta F/F_0$ of plasma membrane Ca^{2+} indicator GCaMP6f in the region of interest (ROI) shown in C of day 1 adult animals expressed neuronal PM-GCaMP6f and ADF presynaptic vesicle marker *(ythEX762[xbx-1p::PM-GCaMP6f; srh-142p::Scarlet::rab-3+unc-119(+)])* with WT; neuronal *cox-5B* knockdown; *tmbim-2(yth130)*; neuronal *cox-5B* knockdown+*tmbim-2(yth130)* background, respectively. The GCaMP6f signal was imaged for 60 s. **(C)** Representative confocal photomicrographs of animals in B. Presynaptic region of ADF neuron was marked with *rab-3* (magenta). A–C stand for different points in time shown in B. The imaging used Z-planes. Scale bar, 2 µm. **(D)** Quantification of the maximal $\Delta F/F_0$ with GCaMP6f signal in ROI shown in B. $n \geq 15$ worms. **(E)** Quantification of the frequency with GCaMP6f fluorescence intensity changes in ROI shown in B. $n \geq 20$ worms. **(F)** Representative fluorescence traces of average background-subtracted fluorescence intensity $\Delta F/F_0$ of mitochondrial Ca^{2+} indicator GCaMP6f in the region of interest (ROI) shown in G of day 1 adult animals expressed neuronal mito-GCaMP6f and ADF presynaptic marker *(ythEX761[xbx-1p::mtLS-GCaMP6f; srh-142p::Scarlet::rab-3+unc-119(+)])* with WT; neuronal *cox-5B* knockdown; *tmbim-2(yth130)*; neuronal *cox-5B* knockdown+*tmbim-2(yth130)* background, respectively. The GCaMP6f signal was imaged for 120 s. **(G)** Representative confocal photomicrographs of animals in F. Presynaptic region of ADF neuron was marked with *rab-3* (magenta). A–C stand for different points in time shown in F. The imaging used Z-planes. Scale bar, 2 µm. **(H)** Quantification of the maximal $\Delta F/F_0$ with GCaMP6f signal in ROI shown in F. $n \geq 15$ worms. **(I)** Quantification of the frequency with GCaMP6f signal in ROI shown in F. $n \geq 20$ worms. **(J)** Representative fluorescence traces of average background-subtracted fluorescence intensity $\Delta F/F_0$ of cytosolic Ca^{2+} indicator GCaMP6f of WT and neuronal *cox-5B* knockdown animals in the 60 s. **(K)** Representative confocal photomicrographs of animals in J. Presynaptic region of ADF neuron was marked with *rab-3* (magenta). A–C stand for different points in time shown in J. The imaging used Z-planes. Scale bar, 2 µm. **(L)** Quantification of the maximal $\Delta F/F_0$ with GCaMP6f signal in ROI shown in J. $n \geq 15$ worms. **P < 0.01; *P < 0.05; ns denotes P > 0.05 via unpaired two-tailed Student's *t* test. Error bars, SEM.

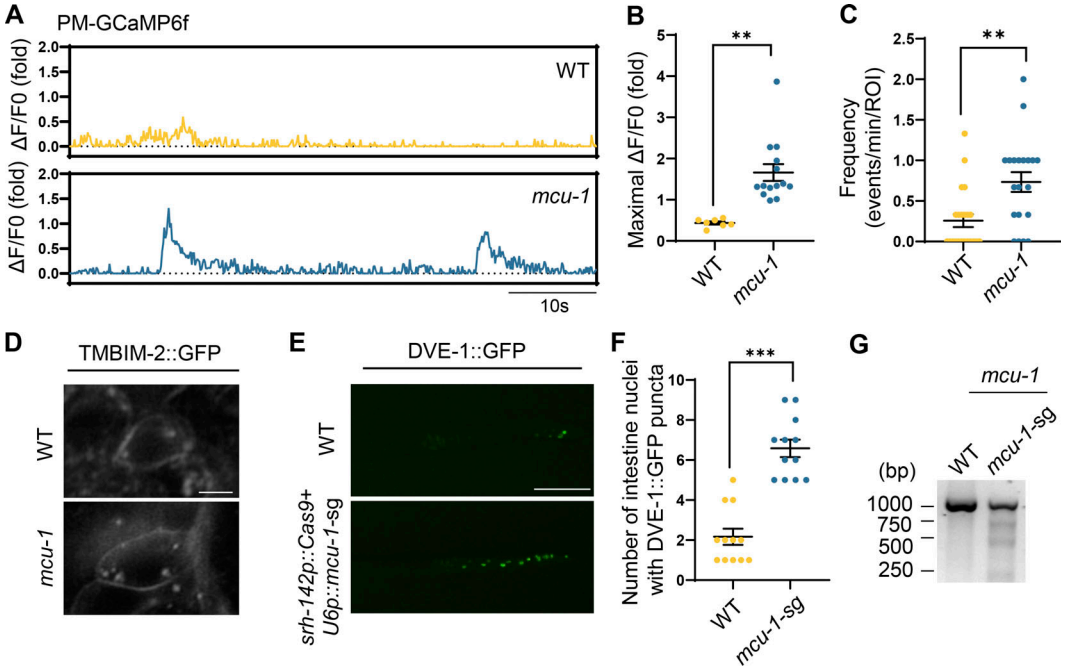

Figure 4. **Loss of *mcu-1* triggers plasma-membrane Ca^{2+} oscillations within synapses of ADF neurons and activates intestinal UPR^{mt}. (A)** Representative fluorescence traces of average background-subtracted fluorescence intensity ΔF/F0 of plasma membrane Ca^{2+} indicator GCaMP6f of WT and *mcu-1(ju1154)* mutant animals in the 60 s. **(B)** Quantification of PM-GCaMP6 maximal fluorescence intensity changes in WT and *mcu-1(ju1154)* animals. $n \geq 8$ worms. **(C)** Quantification of the frequency with GCaMP6f fluorescence intensity changes in WT and *mcu-1(ju1154)* animals. $n \geq 20$ worms. **(D)** Representative confocal photomicrographs of TMBIM-2::GFP animals with the presence or absence of *mcu-1(ju1154)*. The imaging used z-planes. Scale bar, 10 µm. **(E)** Representative photomicrographs of *dve-1* reporter expression in WT and ADF neuron *mcu-1* knockdown animals (*srh-142p::Cas9+u6p::mcu-1 sgRNA*). Scale bar, 250 µm. **(F)** Quantification of the number of intestinal nuclei puncta with GFP signal per worm in E. $n \geq 12$ worms. **(G)** Deletions of *mcu-1* by CRISPR/Cas9 are detected by T7E1 assay. Representative DNA gels of T7E1 assay show *mcu-1* PCR products amplified from genomic DNA of WT or *srh-142p::Cas9+u6p::mcu-1-sg* worms. ***P < 0.001; **P < 0.01 via unpaired two-tailed Student's *t* test. Error bars, SEM. Source data are available for this figure: SourceData F4.

proximity to synaptic clusters of GLR-1, facilitating neuronal excitation by supporting calcium signaling and synaptic activity (Doser et al., 2024).

To investigate this, we observed the Ca^{2+} dynamics near the plasma membrane at the synapse of ADF neurons in *mcu-1* mutant worms with defects in mitochondrial Ca^{2+} import. Intriguingly, *mcu-1* mutants exhibited pronounced increases in the amplitude and frequency of PM-GCaMP6f Ca^{2+} waves (Fig. 4, A–C). Moreover, the *mcu-1* mutants led to the induction of TMBIM-2 expression (Fig. 4 D). To explore the role of *mcu-1* in ADF neurons for neuronal-to-intestinal UPR^{mt} activation, we generated transgenic worms with CRISPR/Cas9-mediated knockout of *mcu-1* in ADF neurons. We found that the *mcu-1* knockout within ADF neurons resulted in the activation of intestinal UPR^{mt} (Fig. 4, E–G; and Fig. S4, C and D), suggesting a direct link between neuronal mitochondrial calcium balance and the activation of intestinal UPR^{mt}. We also observed that *mcu-1* knockdown-triggered Ca^{2+} oscillations are also dependent on TMBIM-2 (Fig. S4, E and F). Additionally, overexpressing MCU-1 within neurons, aimed at enhancing mitochondrial calcium buffering capacity, attenuated UPR^{mt} activation in neuronal Q40::YFP worms (Fig. S4, A and B). These findings highlight the pivotal role of mitochondrial calcium buffering capacity in shaping intracellular calcium signaling dynamics and orchestrating intertissue stress communication.

TMBIM-2 acts with the calcium pump MCA-3 to mediate cell non-autonomous UPR^{mt} activation

Despite the established role of TMBIM family proteins in maintaining Ca^{2+} equilibrium within cells (Liu, 2017), the molecular mechanism of TMBIM2 is unclear. To investigate the molecular function of TMBIM-2, we performed immunoprecipitation (IP) experiments on *C. elegans* expressing TMBIM-2::GFP, followed by mass spectrometry (MS) to identify TMBIM-2 interaction partners (Fig. 5 A and Table S4). These experiments yielded a variety of membrane-associated proteins. Gene Ontology (GO) analyses of these genes (score >10) highlighted pathways including intracellular protein transport, protein N-linked glycosylation, vesicle docking involved in exocytosis, and notably, calcium ion transport. Among these candidates, calcium ion transport emerged as significantly enriched, with MCA-3 topping the list (Fig. 5 B).

MCA-3 shares homology with a plasma-membrane Ca^{2+}-ATPase (PMCA) that employs ATP hydrolysis to transport Ca^{2+} from the cytosol to extracellular spaces (Brini and Carafoli, 2011). Elevated Ca^{2+} levels within neurons give rise to a range of detrimental consequences, including compromised synaptic plasticity, excitotoxicity, mitochondrial dysfunction, and apoptosis (Berliocchi et al., 2005). To counteract increased Ca^{2+} levels, neurons employ a multifaceted approach involving pumps, transporters, cytoplasmic calcium-binding proteins, and buffering by mitochondria

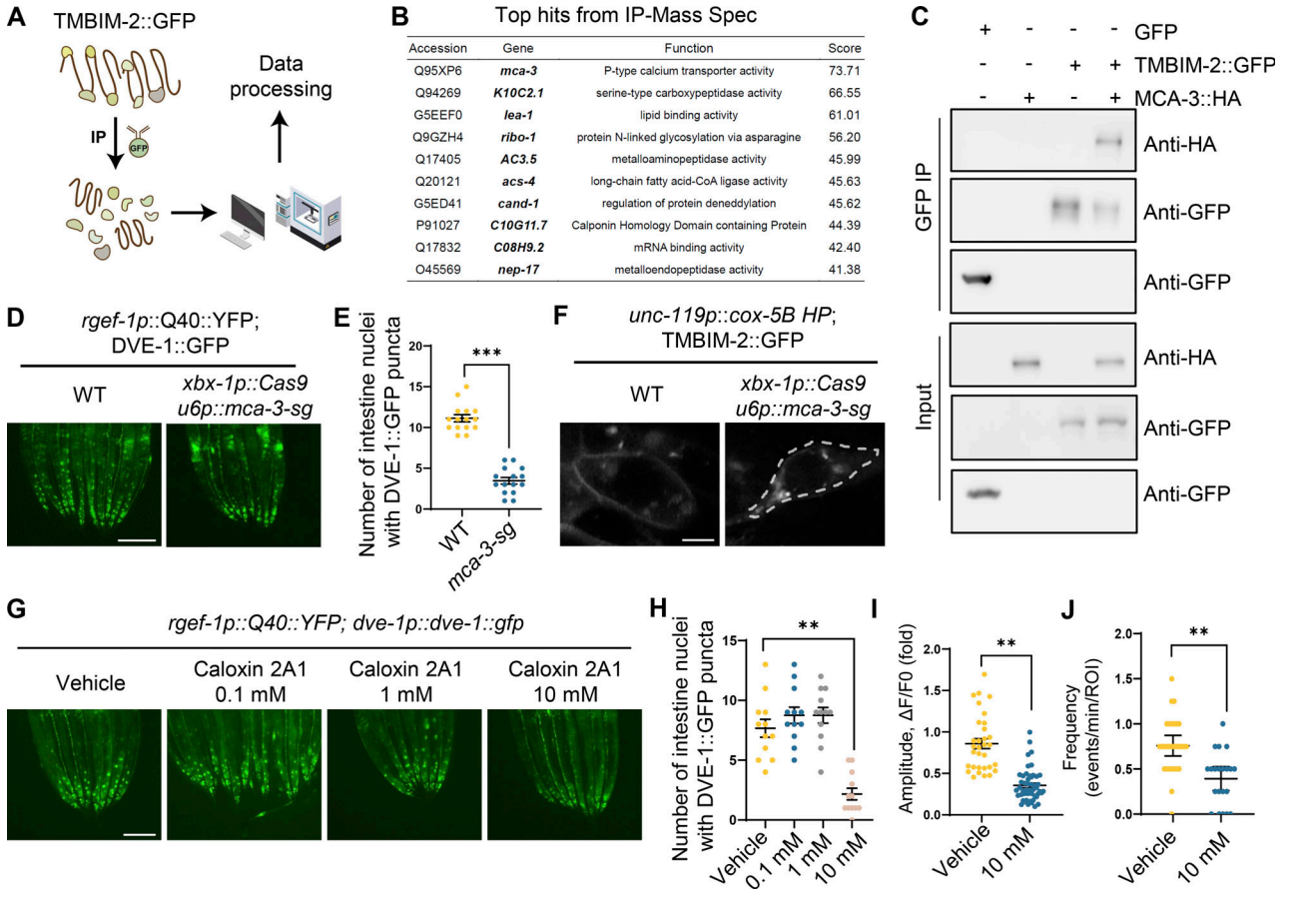

Figure 5. **TMBIM-2 acts with the calcium pump MCA-3 in regulating cell non-autonomous UPR^{mt} activation. (A)** Workflow of the IP-MS method in expression TMBIM-2::GFP *C. elegans*. **(B)** List of TMBIM-2–interacting proteins that top 10 candidates identified by IP-MS experiments. **(C)** Interactions of TMBIM-2 with MCA-3. HEK293T cells transfected with the indicated cDNAs and followed by the indicated immunoprecipitations. **(D)** Representative photomicrographs of ciliated neuronal knockout of *mca-3* in neuronal Q40::YFP, *dve-1p::dve-1::gfp* worms. Scale bar, 250 µm. **(E)** Quantification of the number of intestinal nuclei puncta with GFP signal per worm as shown in D. $n \geq 15$ worms. **(F)** Fluorescence images of neurons in strains expressing TMBIM-2::GFP with the presence or absence of ciliated neuronal knockout of *mca-3*. Scale bar = 2 µm. **(G)** Representative photomicrographs of *dve-1p::dve-1::gfp* reporter in neuronal Q40::YFP animals with PMCA inhibitor Caloxin 2A1, respectively. Scale bar, 250 µm. **(H)** Quantification of the number of intestinal nuclei puncta with GFP signal per worm as shown in G. $n \geq 10$ worms. **(I)** Quantification of PM-GCaMP6 maximal fluorescence intensity changes in animals with a vehicle and 10 mM Caloxin 2A1. $n \geq 20$ worms. **(J)** Quantification of the frequency with GCaMP6f fluorescence intensity changes in animals with a vehicle and 10 mM Caloxin 2A1. $n \geq 20$ worms. ***P < 0.001; **P < 0.01 via unpaired two-tailed Student's *t* test. Error bars, SEM. Source data are available for this figure: SourceData F5.

(Berridge et al., 2003; Devine and Kittler, 2018; Nanou and Catterall, 2018). To explore the potential interactions between TMBIM-2 and MCA-3, we conducted co-immunoprecipitation experiments using HEK293T cells overexpressing *C. elegans* TMBIM-2::GFP and MCA-3::HA. Our results showed an interaction between TMBIM-2 and MCA-3 (Fig. 5 C).

We generated tissue-specific *mca-3* knockdown mutants using CRISPR/Cas9 gene editing. Remarkably, the knockdown of *mca-3* specifically in ciliated sensory neurons, robustly suppressed intestinal UPR^{mt} activation in animals expressing neuronal Q40::YFP (Fig. 5, D and E; and Fig. S4, G–I). It was noted that the loss of *mca-3* also attenuated the enrichment of TMBIM-2::GFP on the plasma membrane (Fig. 5 F), suggesting a dependency of MCA-3 and calcium balance on the subcellular localization of TMBIM-2. We found that the expression of *mca-3* significantly increased with aging and the expression of *mca-3* also significantly increased under neuronal mitochondrial stress (Fig. S4, J and K).

Having established that genetic ablation of *mca-3* suppressed intestinal UPR^{mt} activation, we further investigated whether pharmacological inhibition of MCA-3 could result in a similar phenotype. We performed experiments using Caloxin 2A1, a specific inhibitor of the plasma membrane Ca^{2+}-ATPase (PMCA). Caloxin 2A1 selectively inhibits the Ca^{2+}-Mg^{2+}–ATPase activity of PMCA without affecting other ATPase, such as Mg^{2+}-ATPase or Na^{+}-K^{+}–ATPase and has been well-characterized in prior studies (Chaudhary et al., 2001; Holmes et al., 2003; Pande et al., 2005, 2008; Szewczyk et al., 2010). Treatment with 10 mM Caloxin 2A1 markedly suppressed intestinal UPR^{mt} activation (Fig. 5, G and H; and Fig. S4, L and M). Additionally, we observed a significant reduction in both the amplitude and frequency of Ca^{2+} waves near the plasma membrane at ADF neuron synapses (Fig. 5, I and J). These results indicate that

TMBIM-2 couples with MCA-3 to mediate Ca^{2+} homeostasis and cell non-autonomous UPR^{mt} in response to mitochondrial perturbations within neurons.

Serotonin supplementation restored the systemic UPR^{mt} activation in *tmbim-2* mutants

Ca^{2+} emerges as a pivotal universal intracellular signaling messenger, intricately regulating vital cellular functions such as cell death, gene transcription, exocytosis, and neuronal transmission (Berridge et al., 2003; Berridge et al., 2000; Carafoli et al., 2001; Pang and Südhof, 2010). By introducing tetanus toxin (TeTx) into neurons—a neurotoxin that inhibits Ca^{2+}-dependent neurotransmitter release (Hendricks et al., 2012), we found that the induction of TeTx in ADF serotoninergic neurons strongly attenuated the intestinal UPR^{mt} activation in animals expressing neuronal *cox-5B* KD or neuronal Q40::YFP expression (Fig. 6, A, B, E, and F; and Fig. S5, A–C), suggesting Ca^{2+}-dependent neurotransmission is required for orchestrating systemic mitochondrial stress communication.

To further explore the neurotransmission under neuronal mitochondrial stress, we used an *srh-142* promoter to drive SNB-1::pHluorin (SpH) expression in the ADF neuron for optical measurements of presynaptic activity, which has been previously validated in *C. elegans* (Han et al., 2017). SNB-1 is an ortholog of human vesicle–associated membrane protein 2 (VAMP2). SNB-1 enables SNAP receptor activity and syntaxin binding activity to mediate chemical synaptic transmission located in the presynaptic active zone. This method involves the quenching of SpH fluorescence in synaptic vesicles (SVs) due to their low/acidic luminal pH. Upon stimulation, neurotransmitter vesicles fuse with the plasma membrane, exposing them to the neutral pH of the extracellular medium, leading to an increase in SpH fluorescence. Notably, under neuronal mitochondrial stress, the fluorescence intensity of SpH increased, indicating enhanced neurotransmitter release (Fig. 6, C and D). Loss of *tmbim-2* significantly suppressed the increase in SpH fluorescence in neuronal *cox-5B* KD worms (Fig. 6, C and D).

Intriguingly, the addition of serotonin effectively restored systemic UPR^{mt} activation in *tmbim-2* mutants as well as in worms expressing TeTx in ADF neurons, in response to neuronal *cox-5B* KD or neuronal Q40::YFP expression (Fig. 6, E and F; and Fig. S5, D–G). Moreover, the expression of *tmbim-2* solely within two ADF sensory neurons was sufficient to induce UPR^{mt} in the intestine (Fig. 6, G and H). This process was dependent upon tryptophan hydroxylase (TPH-1), an enzyme responsible for serotonin synthesis (Sze et al., 2000) (Fig. 6, G and H). Furthermore, electron micrograph ultrastructural analyses revealed that *tmbim-2* mutants exhibited a significant increase in the number of synaptic vesicles at active zones of neurons (Fig. S5, H and I), while the vesicle diameter remained comparable to that of WT worms (Fig. S5, H and J). These findings suggest that TMBIM-2 plays a crucial role in facilitating serotonin release from ADF neurons, thereby enhancing neuronal-to-intestinal mitochondrial stress communication.

Overexpression of TMBIM-2 preserves age-onset decline of aversive learning and extends the lifespan of *C. elegans*

As organisms age, their ability to respond to stress gradually declines. To investigate the role of TMBIM-2 in the aging process, we analyzed published gene expression datasets, revealing a decline in *Tmbim2* expression in the brain with aging (Schaum et al., 2020; Zhang et al., 2013). This pattern mirrored observations in the single-cell atlas study of aging *C. elegans*, where *tmbim-2* mRNA levels decreased in ADF neurons (Fig. 7, A–C and Fig. S5 K). Additionally, the TMBIM-2::GFP protein level in the nervous system and spermatheca of Day 5 worms both exhibited a significant decrease compared with Day 1 worms (Fig. 7, D and E; and Fig. S5, L and M). This decline in TMBIM-2 protein levels during aging is consistent with the gradual decrease in Ca^{2+} oscillations in response to prolonged neuronal mitochondrial stresses (Fig. 7 F).

Neurotransmission is also involved in aversive learning behavior in response to exposure to pathogenic bacteria *Pseudomonas aeruginosa* 14 (PA14). Typically, *C. elegans* is attracted to PA14 initially but learns to avoid it after several hours of exposure, relying on serotonin (Zhang et al., 2005). *tmbim-2* mutants exhibited significantly diminished pathogen-induced aversive learning, as did *tph-1* mutants (Fig. 7, G and H). This reduction in learning capacity was exacerbated in Day 5 worms, who nearly lost their ability to avoid PA14. Intriguingly, the overexpression of TMBIM-2 preserved aversive learning behavior in older worms (Fig. 7, G and I).

Through the life span analysis of *tmbim-2*, we found that *tmbim-2* mutants exhibited a normal lifespan compared with WT worms (Fig. S5 N). However, they significantly suppressed the longevity effect caused by neuronal *cox-5B* KD (Fig. 7 J). Furthermore, TMBIM-2 overexpression extended the lifespan of *C. elegans* (Fig. 7 K). Additionally, overexpression of TMBIM-2 solely in ADF neurons was sufficient to extend the lifespan in *C. elegans* (Fig. S5 O). To assess whether *tmbim-2* mutants or overexpression influences worm survival under *P. aeruginosa* PA14 exposure, we performed survival assays on PA14 lawns using wild-type, tmbim-2 knockouts, and TMBIM-2 overexpression worms. Our results revealed that *tmbim-2* mutants exhibited significantly reduced survival rates, whereas TMBIM-2 overexpression conferred enhanced resistance when exposed to PA14, particularly on day 5, further highlighting its pivotal role in stress resilience (Fig. 7, L and M). These findings suggest that reduced levels of TMBIM2 with age might contribute to age-related neuronal function decline and metabolic dysregulation across species. Overexpression of TMBIM-2 emerged as a potential mechanism to preserve neuronal function in older animals and potentially impact lifespan regulation.

Discussion

The nervous system senses external and internal stimuli and transmits information to coordinate metabolism and behavior essential for overall health and aging (Bar-Ziv et al., 2020; van Oosten-Hawle and Morimoto, 2014). Through our investigation, we uncovered a previously unrecognized interplay: chronic disruption of neuronal mitochondria leads to the initiation of

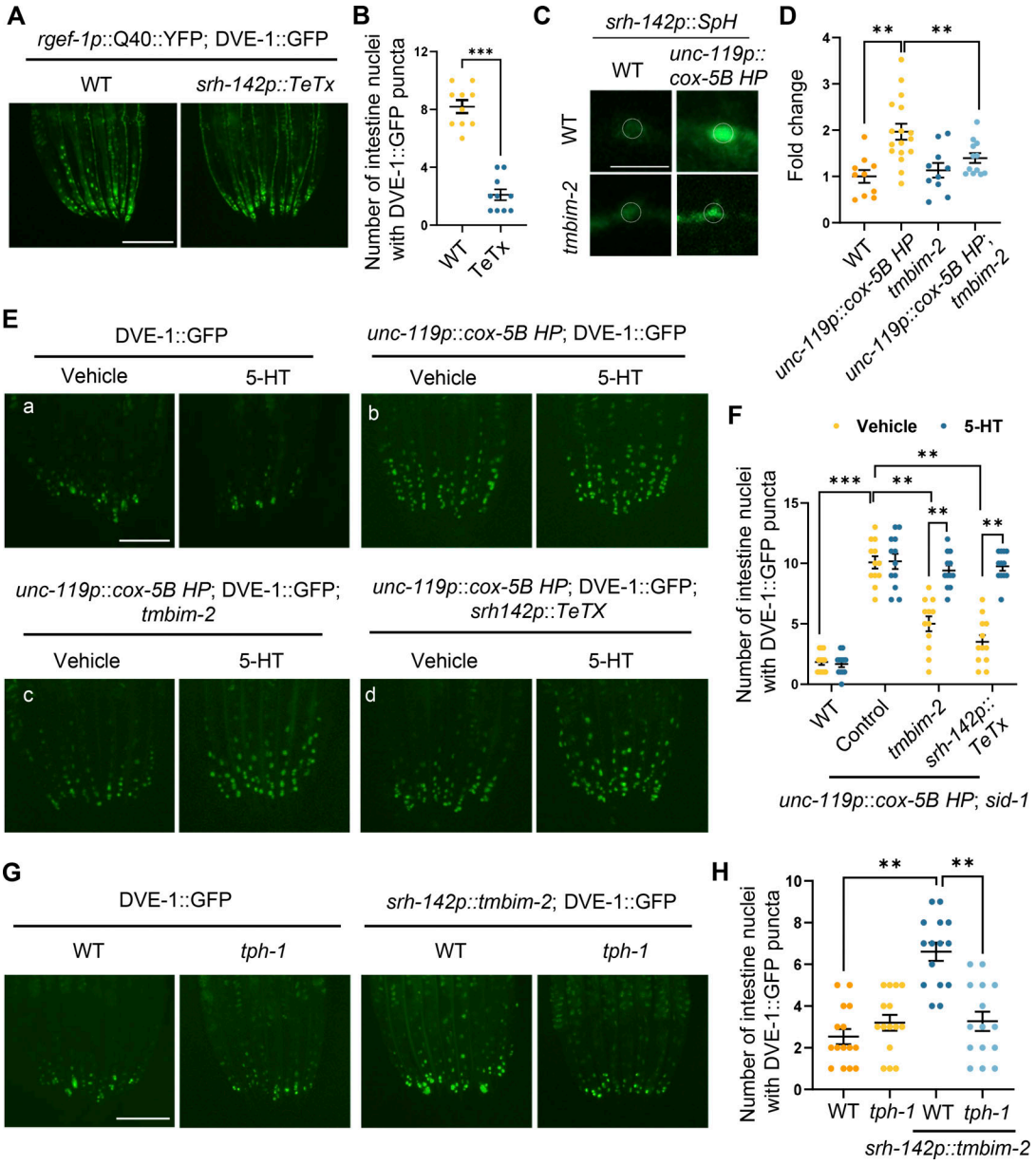

Figure 6. **Supplementation of serotonin restored the neuronal-to-intestinal UPR^{mt} activation in *tmbim-2* mutants. (A)** Representative photomicrographs of *dve-1* reporter in animals expressing neuronal Q40 and neurotoxin TeTx in ADF neuron (*ythEx768[srh-142p::TeTx::sl2::mcherry]*). Scale bar, 250 µm. **(B)** Quantification of the number of intestinal nuclei puncta with GFP signal per worm as shown in A. $n \geq 15$ worms. **(C)** Representative photomicrographs of the ADF neurotransmitter exocytosis reporter (*ythEX766[srh-142p-SYP-Phluorin+unc-119(+)]*) in control or neuronal *cox-5B* knockdown animals in WT or *tmbim-2(yth130)* background. The imaging used Z-stacks. Scale bar, 2 µm. **(D)** Quantification of *srh-142p::snb-1::pHluorin* fluorescence in the neurons of animals as depicted in C: WT (orange); *tmbim-2(yth130)* (yellow); *unc-119p::cox-5B HP* (ultramarine); *unc-119p::cox-5B; tmbim-2(yth130)* (wathet). $n \geq 12$ worms. **(E)** Representative photomicrographs of *dve-1* reporter expression in WT **(a)**; neuronal *cox-5B* knockdown **(b)**; neuronal *cox-5B* knockdown; *tmbim-2* **(c)**; neuronal *cox-5B* knockdown; or ADF neuron overexpressing TeTx(*ythEX768[srh-142p::TeTx::sl2::mCherry+unc-119(+)];unc-119(ed-3)III*) **(d)** animals treated with vehicle control or 50 mM serotonin (5-HT). **(F)** Quantification of the number of intestinal nuclei puncta with GFP signal per worm as shown in E, yellow for control and blue for feeding 5-HT. $n \geq 12$ worms. Statistical analysis was performed by ANOVA followed by Tukey post-hoc test (**P < 0.01; ***P < 0.001). **(G)** Representative photomicrographs of *dve-1* reporter in control or ADF neuron overexpressing TMBIM-2 animals in WT or *tph-1(n4622)* background. **(H)** Quantification of the number of intestinal nuclei puncta with GFP signal per worm as shown in G. $n \geq 15$ worms. ***P < 0.001; **P < 0.01 via unpaired two-tailed Student's *t* test. Error bars, SEM; Scale bar, 250 µm.

tmbim-2–dependent spatiotemporal Ca^{2+} wave dynamics. These dynamic Ca^{2+} oscillations might facilitate enhanced serotonin release, which, in turn, governs systemic mitochondrial stress response regulation and aging processes (Fig. 8). These results suggest a more intricate connection between mitochondrial function and neurotransmission, operating at a subtle but continuous level beneath the threshold of global intracellular Ca^{2+} signals.

The universal presence of TMBIM protein across prokaryotes, fungi, animals, and humans implies their crucial role in

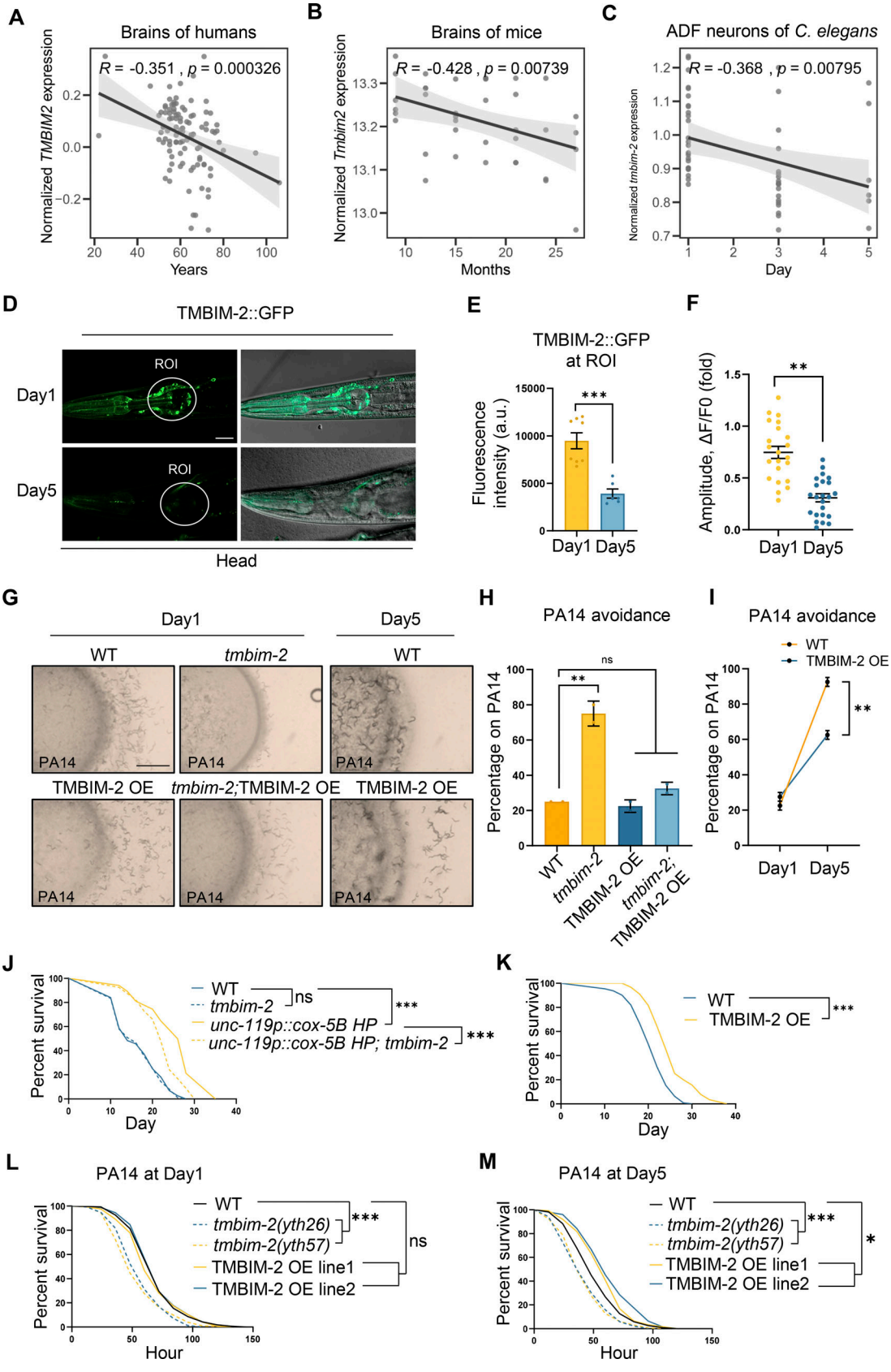

Figure 7. **Overexpression of TMBIM-2 in neurons preserves age-onset decline of aversive learning of *C. elegans*. (A)** Correlation between normalized expression of *Tmbim2* in the prefrontal cortex of human brains with Alzheimer's disease at different ages. Expression values in A (n = 101 samples) are from the dataset GSE44772. **(B)** Correlation between normalized expression of *Tmbim2* in mouse brains at different ages. Expression values are from the dataset

GSE132040 (n = 38 samples). **(C)** Correlation between normalized expression of *srh-142* positive neurons at different ages. Expression values are from Roux et al. (2023) (n = 147 cells). **(D)** Representative confocal photomicrograph of animals head expressing TMBIM-2 at different ages. The imaging used z-planes. Scale bar, 20 µm. **(E)** Quantitative analysis of TMBIM-2::GFP protein levels in ROI shown in D. $n \geq 8$ worms. **(F)** Quantification of the amplitude of PM-GCaMP6f fluorescence intensity changes in expressed neuronal PM-GCaMP6f and ADF presynaptic vesicle marker worms with neuronal *cox-5B* knockdown at different ages. **(G)** Example of control and aversion phenotypes after exposure to pathogenic *P. aeruginosa* PA14 in WT, *tmbim-2*, *tmbim-2p::tmbim-2::gfp* and *tmbim-2*; *tmbim-2p::tmbim-2::gfp* animals at day 1. Scale bar, 250 µm. **(H)** Quantification of the percentage of the worm on PA14 at day 1 as shown in G. n = 2 independent experiments. **(I)** Quantification of the percentage of the worm on PA14 in WT and *tmbim-2p::tmbim-2::gfp* animals at day 5 as shown in G. n = 2 independent experiments. **(J)** Survival analyses of WT (solid blue); *tmbim-2* (dashed blue); *unc-119p::cox-5B HP* (solid yellow) and *unc-119p::cox-5B HP*; *tmbim-2* (dashed yellow) animals; $n \geq 100$ worms. **(K)** Survival analysis of WT (blue) and *tmbim-2p::tmbim-2::gfp* (yellow); $n \geq 100$ worms. **(L)** PA14 survival analyses of WT (black), *tmbim-2 (yth26)* (dashed blue), *tmbim-2 (yth57)* (dashed yellow), TMBIM-2 overexpression line1 (solid blue), and TMBIM-2 overexpression line2 (solid yellow) at day1 adult animals; $n \geq 100$ worms. **(M)** PA14 survival analyses of WT (black), *tmbim-2 (yth26)* (dashed blue), *tmbim-2 (yth57)* (dashed yellow), TMBIM-2 overexpression line1 (solid blue), and TMBIM-2 overexpression line2 (solid yellow) at day5 adult animals; $n \geq 100$ worms. ***P < 0.001, **P < 0.01, *P < 0.05, ns denotes P > 0.05 via unpaired two-tailed Student's t test. Error bars, SEM. In A–C, we used Pearson's correlation coefficient for statistical testing. In J–M, we used The Log-rank (Mantel-Cox) test for statistical analysis.

preserving Ca^{2+} homeostasis throughout evolution (Chang et al., 2014; Liu, 2017). At the subcellular level, TMBIM2 is found in lipid rafts of the plasma membranes, endoplasmic reticulum, and Golgi apparatus, aligning with *tmbim-2* expression in *C. elegans* (Rojas-Rivera and Hetz, 2015). This observation supports the notion that TMBIM2 is a conserved member of the TMBIM protein family, and its subcellular distribution and trafficking are critical for bridging its function with localized Ca^{2+} homeostasis. The unique structure of BsYetJ (or TMBIM6) suggests its potential as intrinsic Ca^{2+} channels, playing a pivotal role in preventing intracellular Ca^{2+} store overload (Chang et al., 2014; Li et al., 2020a).

According to AlphaFold prediction, TMBIM-2 consists of a free peptide segment at the N-terminal, followed by seven transmembrane regions. Previous studies have suggested that the seventh transmembrane region of TMBIM family proteins may play a crucial role in regulating calcium homeostasis regulation, with potential conformational changes occurring under varying conditions (Bultynck et al., 2012). The *yth57* mutant, identified through EMS mutagenesis screening, harbors a mutation in the seventh transmembrane region, potentially explaining why point mutations exhibit a phenotype akin to null alleles. Further investigation into the structure of TMBIM-2 holds promise for enhancing our comprehension of its role in regulating Ca^{2+} equilibrium. Our IP-MS study identified that TMBIM-2 acts with the Ca^{2+} pump MCA-3, enabling efficient Ca^{2+} export after rapid Ca^{2+} elevation. This accelerates the recovery to an equilibrium concentration, allowing for long-lasting synaptic modifications. The PMCA pumps are characterized by their high affinities and modest transport rates. This interplay facilitates both rapid and sustained vesicle release and enduring alterations in neuronal activity. Mechanisms governing TMBIM-2's interacting calcium pumps, like MCA-3, warrant further exploration to comprehend their role in achieving Ca^{2+} equilibrium.

Contrary to the conventional perspective that associates mitochondrial dysfunction with diminished ATP production and compromised neurotransmission (Li and Sheng, 2022; Li et al., 2020b), our study presents a contrasting view. Emerging data have shown that transient mitochondrial stress, such as mitochondrial depolarization, MCU ablation, or inhibiting permeability transition pore (mPTP), can augment synaptic transmission in mouse neurons (Kwon et al., 2016; Levy et al., 2003; Marland et al., 2016; Tang and Zucker, 1997). Moreover, our study revealed the mechanism by which prolonged mitochondrial perturbations lead to sustained, TMBIM-2–dependent Ca^{2+} wave alterations in vivo. This, in turn, possibly allows for neurotransmission, influencing long-term metabolic control and playing a crucial role in the aging process.

The ability of neurons to dynamically respond to changing intracellular Ca^{2+} signaling demands, spanning from minutes to days, weeks, and longer, underscores the necessity for precise control over Ca^{2+} transporter type, localization, and activity (Berridge et al., 2003). Understanding the intricate link between mitochondrial function and Ca^{2+} signaling in neurotransmission, particularly within the context of diverse cellular stresses during aging, is imperative. Given the predominant expression of mammalian TMBIM2 in the adult central nervous system and the observed diminished responsiveness to Ca^{2+} upon mitochondrial stresses with age in *C. elegans* (Reich et al., 2011; Schweitzer et al., 2002; Tauber et al., 2014), restoring Ca^{2+} equilibrium could emerge as a promising therapeutic strategy to enhance neuronal function and regulate organismal metabolism during the aging process.

Materials and methods

C. elegans maintenance and transgenic lines

Nematodes *C. elegans* strains were obtained from the Caenorhabditis Genetics Center (CGC) or the National Bioresource Project (NBRP). *C. elegans* were maintained and experimentally examined at 20°C on standard nematode growth medium (NGM) agar plates seeded with *Escherichia coli* OP50 unless otherwise stated (Brenner, 1974). The strains used in this study are listed in Table S1.

Mutagenesis screen and gene mapping

This protocol for ethyl methane sulfonate (EMS) mutagenesis screening and gene mapping was described previously (Li et al., 2022). About 120 L4 worms were treated with the final concentration of EMS to 47 mM and incubated at 20°C on a spinning wheel for 4 h. Worms washed with M9 buffer three times were transferred to NGM plates. A selection of healthy L4 animals was made to become P0. F1 progeny were self-fertilized, and F2 animals were screened for the phenotype of interest.

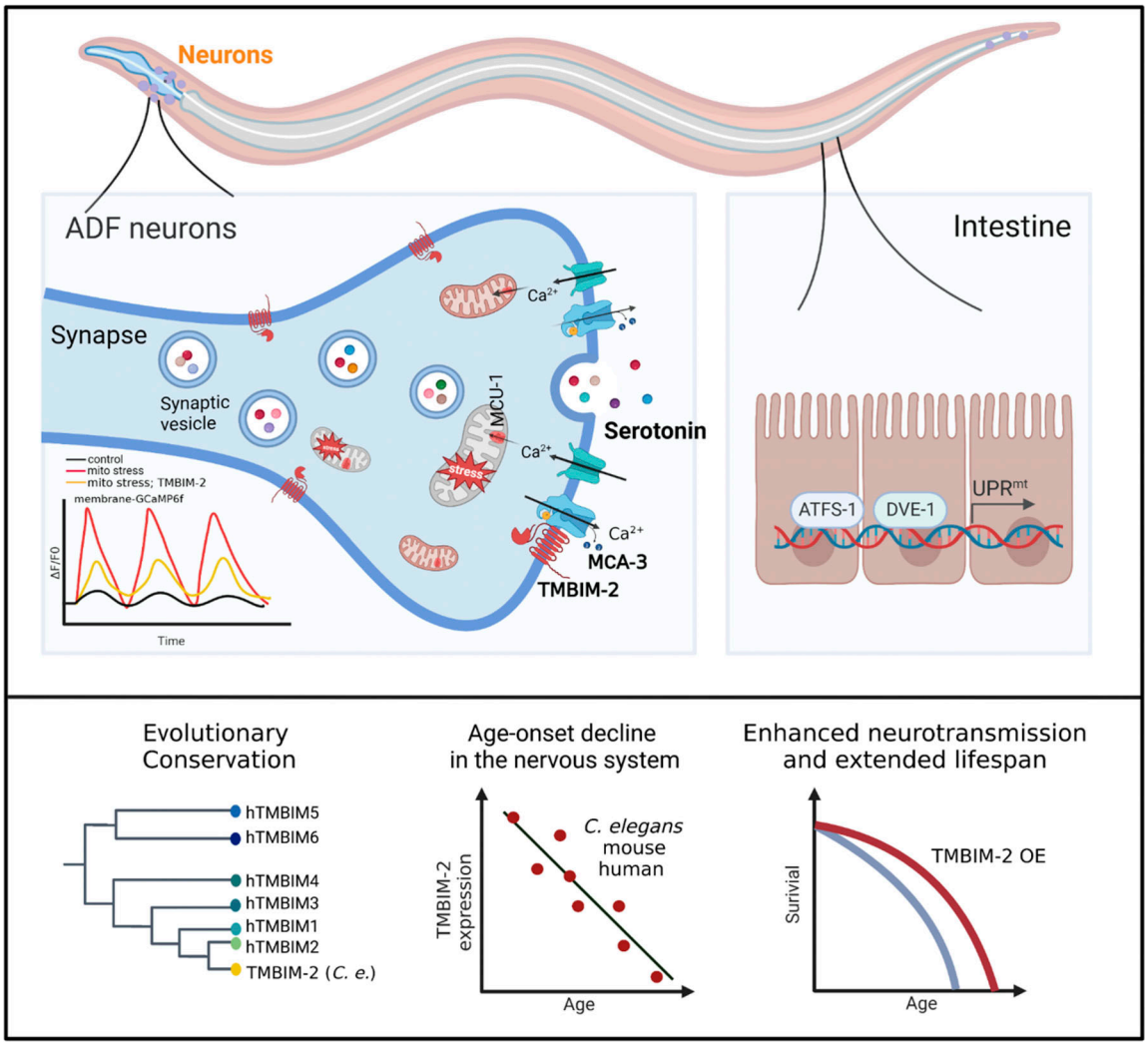

Figure 8. **Model of chronic mitochondrial stress leads to *tmbim-2*-dependent spatiotemporal Ca^{2+} waves to coordinate neuronal-to-intestinal UPR^{mt} activation and aging.** Persistent disturbances in neuronal mitochondrial function induce TMBIM-2-dependent calcium (Ca^{2+}) oscillations, fostering the release of neurotransmitters to orchestrate a systemic response to mitochondrial stress. Notably, TMBIM2 expression diminishes with aging in neurons across diverse organisms, including *C. elegans*, mice, and humans. Intriguingly, augmenting TMBIM2 levels through overexpression demonstrates a protective effect against age-related deterioration in aversive learning and imparts an extended lifespan in *C. elegans*. These findings underscore the pivotal role of TMBIM-2 in mediating the interplay between chronic neuronal mitochondrial perturbations, calcium dynamics, and the broader physiological responses associated with aging.

After being outcrossed with the *rgef-1p::egl-20; dve-1p::dve-1::gfp* animals at least three times, the mutants were subjected to the whole-genome sequencing. Meanwhile, the mutants were crossed with animals expressing *rgef-1p::egl-20; dve-1p::dve-1::gfp* in CB4856 (Hawaiian) background. Then single nucleotide polymorphism (SNP) mapping was described previously (Davis et al., 2005). Through canonical SNP mapping and whole genome sequencing, we found a *yth57* mutation located in the gene *xbx-6*.

Plasmid construction

The 3.7 kb promoter region of *tmbim-2*, the *tmbim-2* genome sequence (2,177 bp) without a stop codon, and a plasmid containing a GFP tag were utilized to construct *tmbim-2p::tmbim-2::GFP* for overexpressing TMBIM-2 in worms. To generate rescue strains, we substituted the *tmbim-2* promoter with various promoters including *rgef-1*(3.3 kb), *gly-19* (1.5 kb), *xbx-1*(1.7 kb), *mec-7*(1.5 kb), *tph-1*(s)(1.5 kb), *tph-1(l)*(2.5 kb), and *srh-220* (2.5 kb) promoter in the *tmbim-2p::tmbim-2* plasmid.

For the strains utilized for calcium imaging, the ciliated-neuron promoter *xbx-1p* was linked with GCaMP6f to generate cytoplasmic GCaMP6f. Additionally, to create GCaMP6f expressed in the plasma membrane and mitochondria, two kinds of subcellular localization sequences, myr (plasma membrane) and mtLS (mitochondria), were inserted at the 5′end of GCaMP6f.

Primer sequences are shown below: *tmbim-2* 3,788 bp promoter: fwd 5′-AAACATCCCTAATCCGCCG-3′, rev 5′-ATCTGG AATTAAATAATATTATTGAAACG-3′; *xbx-1* 1,695 bp promoter: fwd 5′-ATCAATGTCCGCCAGCTTAC-3′, rev 5′-ACTAATAAA TTGAGCAATATTGGAG-3′; *osm-6* 3,316 bp promoter: fwd 5′-ACGATGGTGTAACTGGTACG-3′, rev 5′-AGATGTATACTAATG

AAGGTAATAGCTTG-3′; *srh-142* 3,996 bp promoter: fwd 5′-CTT TCATAATCCAGCGGCTTTCC-3′, rev 5′-ATTGGCAAAAAGAAA AAAGAGGTGC-3′.

C. elegans CRISPR transgenics

The *tmbim-2* mutant worms were created using CRISPR/Cas9 technology following published protocols (Waaijers et al., 2013). *tmbim-2 (yth26)* and *tmbim-2(yth130)* were generated using three guide RNA sequences (5′-TTCTGATAAGCCGGGTTGTA-3′, 5′-CAATCAACAGCCATACAACC-3′, and 5′-CAGAATCCCTACCCC AATCA-3′). sgRNA of *tmbim-2* was cloned into the pDD162 vector with the expression of Cas9. The plasmid (50 ng/µl) was injected into N2 with the coinjection marker *myo-2p::tdTomato* (10 ng/µl). Single F1 worms with the expression of coinjection marker were picked into new plates, and the F2 progeny were examined by PCR amplification and confirmed by sequencing.

To generate knockout specifically in ciliated neurons or ADF neurons, the *eft-3* promoter in the original vector was replaced with *osm-6* (3,289 bp preceding exon1) or *srh-142* (3,996 bp preceding exon1) promoter to express Cas9 endonuclease specifically in ciliated neurons or ADF neurons. *ADFp::Cas9+U6p::mcu-1* sgRNA constructs were generated using guide RNA sequence (5′-GATCCGATTGTGTCACTGAG-3′) with the *srh-142* promoter and Cas9. F2 progeny were examined by T7 endonuclease I (T7E1) assay, which was performed to detect indels (Mashal et al., 1995; Shao et al., 2016).

RNAi feeding

Knockdown by RNA interference (RNAi) of indicated genes was conducted by feeding worms the *E. coli* strain HT115 expressing double-stranded RNA homologous to the target genes. The RNAi feeding protocol used was described previously (Zhang et al., 2018). Synchronized worms were bleached with a bleaching buffer (1.5% NaClO; 0.65 M KOH) and grown from hatching on *E. coli* HT115 strains containing an empty vector control or double-stranded RNA bacteria. The L4440 empty vector served as a negative control. *E. coli* carrying the appropriate vectors were cultured in LB broth supplemented with ampicillin (100 mg/ml) at 37°C overnight and plated onto NGM plates containing 100 mg/ml ampicillin and 3 mM isopropyl b-D-thiogalactoside (IPTG) (RNAi plates). RNAi-expressing bacteria were allowed to grow for 2–3 days. RNAi strains were obtained from the Vidal library and Ahringer library.

Microscopy and image analysis

For imaging the activation of UPR^{mt} in *C. elegans*, eight to ten worms were anesthetized using sodium azide (NaN3) (50 mM) before imaging. Whole-worm micrographs were acquired using a Leica M165 FC dissecting microscope equipped with a 6.3× objective and LAS X software (Leica) at 20°C. Acquisition parameters were maintained constant among all samples, and all images presented are representative of more than three images. For quantifying the nuclear localization of DVE-1::GFP, worms were mounted on agarose pads and imaged using a Zeiss Imager M2 microscope. The intensity of GFP fluorescence for the *hsp-6p::gfp* reporter was quantified by outlining the entire region of the intestine and analyzing it using ImageJ software. Acquisition settings were consistent across genotypes for quantitative analysis.

For the observation of neurons in *C. elegans*, animals were mounted on 2% agarose pads made in M9 medium, immobilized using 0.05% levamisole hydrochloride, and placed under a coverslip (Chung et al., 2013). Worms at the day 1 stage were mounted on 5% agarose pads and imaged using a Zeiss Imager LSM980 with Airyscan 2 Laser Scanning Confocal microscope equipped with a 63×/1.40 Oil DIC objective controlled by the ZEN software (Carl Zeiss) at 20°C The excitation/emission wavelengths for GFP and mCherry are 488/505–530 nm and 543/560–600 nm, respectively. To record the colocalization of the two fluorescent proteins (GFP and mCherry) in neurons, images of the two channels were captured simultaneously to avoid possible shifts due to movements, rather than sequentially. For each image, the same region of interest (ROI) was used at the same focal plane. The intensity of GFP fluorescence for the SpH reporter was quantified by outlining the ROI of the synapse and analyzing it using ImageJ software. The anesthetic of SpH reported strain was 0.05% levamisole hydrochloride. Acquisition settings were consistent across genotypes for quantitative analysis.

For imaging the plasma membrane of *C. elegans* neurons, we used the multi-SIM system that integrates TIRF-SIM, grazing incidence (GI-SIM), and 3D-SIM, as well as lattice light sheet microscopy (LLSM) (Guo et al., 2018; Zheng et al., 2022). Single-Slice-SIM images of the plasma membranes of ADF neurons in *C. elegans* were acquired on the Multi-SIM imaging system (NanoInsights) with a 100×/1.49 NA oil objective (Nikon CFI SR HP Apo), solid-state lasers (488 and 561 nm), and an sCMOS (complementary metal-oxide-semiconductor) camera (Photometrics Kinetix) at 20°C. To obtain optimal images, immersion oils with refractive indices of 1.518 were used for *C. elegans* on glass coverslips. The microscope was routinely calibrated with 100 nm fluorescent spheres to calculate both the lateral and axial limits of image resolution. SIM image stacks were reconstructed using SI-Recon 2.23.3 (NanoInsights) with the following settings: pixel size 30.6 nm; channel-specific optical transfer functions; Wiener filter constant 0.01 for 2D mode and 0.005 for 3D mode; and discard negative intensities background. Then the reconstructed SIM image was denoised with total variation (TV) constraint. Pixel registration was corrected to be <1 pixel for all channels using 100 nm fluorescence beads. Multi-SIM images were analyzed by Image J.

DID staining

Uptake of 1,1′-dioctadecyl-3,3,3,3-tetramethylindodicarbocyanine (DiD) to identify a subset of amphid sensory neurons capable of dye uptake was assayed as described previously (Mills et al., 2016). Briefly, a stock solution (1 mM) of DiD was diluted 1:200 in M9 buffer. Larval stage 4 (L4) animals were incubated in 200 µl of diluted DiD for 1 h at room temperature, transferred to a fresh nematode growth medium seeded with OP50, and then placed on agarose pads with sodium azide for visualization.

Calcium imaging

Calcium imaging was conducted in *C. elegans* following a previously described protocol (Chung et al., 2013). Adult day

1 animals were selected for imaging. A 0.05% Levamisole solution was added to 2% agarose pads. Subsequently, three animals were picked onto the pad and covered with a coverslip. Small amounts of the hot wax mixture (50% paraffin wax and 50% petroleum jelly) were applied to the corners of the coverslip to hold it in position. After allowing 3–5 min for the Levamisole to take effect and one animal to become completely still, imaging was performed.

All videos were captured using a Zeiss LSM 980 microscope equipped with an Airyscan 2 and a 63×/1.40 Oil objective in a multiplex SR-4Y Mode. GCaMP6f was excited with 488 nm light at a laser intensity of 3.5%, Scarlet was excited with 568 nm light at a laser intensity of 0.5%. Animals were imaged at 10 Hz for 1 min at 20°C. All videos were recorded under identical experimental parameters, including the same pixel size, laser intensity, multiplex mode, and gain value. The analysis focused on axonal synapses in the neuronal ring region of ADF neurons. Only animals that survived the imaging protocol were included in the study.

GCaMP6f fluorescence was analyzed as follows: mean background fluorescence was subtracted from the mean fluorescence in the region of interest (ROI). The baseline fluorescence in the ROI was determined by performing a linear regression of the entire video and subtracting it from the raw ROI data. This baseline was used to correct fluorescence signals within the ROI for photobleaching during the experiment. $\Delta F/F_0$ was calculated using the formula $(F–F_0)/F_0$.

TEM analysis

Adult *C. elegans* (day 1 of adulthood) were frozen by the high-pressure freezer (HPM100; Leica). Subsequently, the fast-frozen samples were immersed into a freezing tube containing 2% osmium tetroxide in 100% acetone and placed into the freeze substitution device (Leica EM AFS) at −90°C for 3 days and then slowly warmed to −60°C for 12 h, −30°C for 12 h, and finally to 0°C. Following freezing substitution, acetone was changed three times (15 min intervals) at 0°C and one time at room temperature, and then they were stained in 0.5% UA (in acetone) at 4°C overnight. After that, samples were slowly infiltrated with SPI Pon 812 resin by placing them in mixtures of acetone and resin of different grades (25%, 50%, 75%, and 100% vol/vol). The liquid resin was then polymerized at 60°C for 48 h. Ultrathin sections were cut using an ultramicrotome (EM UC6; Leica) equipped with a diamond knife and placed on a TEM grid. Observation of the samples was performed using transmission electron microscopy (FEI Tacnai Spirit) operating at 100 kV.

Western blot analysis

100 synchronized day-1 adult worms were transferred into a tube containing 16 µl M9 buffer, which were then snap-frozen in liquid nitrogen and kept at −80°C until all the samples were ready for analysis. Cells were lysed either in radioimmunoprecipitation assay (RIPA)-lysis buffer (50 mM Tris-HCl, pH 7.4, 150 mM NaCl, 1% Triton X-100, 1% sodium deoxycholate, 0.1% SDS, and cOmplete EDTA-free Protease Inhibitor Cocktail [05892791001; Roche]) and then subjected to SDS-PAGE. Cells lysed with RIPA-lysis buffer were set on ice for 30 min and then centrifuged at 20,000 *g* for 10 min. The supernatants were then mixed with 5 × SDS buffer, mixed well, and boiled for 15 min. All protein lysates were resolved by 10% Bio-Rad gels and transferred to PVDF membranes. The membranes were further blocked in tris-buffered saline with Tween-20 (TBST) buffer with 5% milk for 1 h and incubated with primary antibodies, which were also diluted in TBST buffer with 5% milk at 4°C overnight. After washing with TBST buffer three times and 5 min for each time, membranes were incubated with horseradish peroxidase (HRP) conjugated anti-rabbit or anti-mouse secondary antibody for 1 h at RT. Then the membranes were washed three times with TBST buffer and incubated with high-sig ECL western Blotting substrate (Tanon). The chemiluminescent signals were captured by a chemiluminescence imaging system (Tanon). The quantification analysis of the western blot band was conducted by ImageJ and normalized to the internal control. Antibodies used in western blots include monoclonal anti-GFP (sc-9996; Santa Cruz Biotechnology) (1:1,000), anti-HA (3724; Cell Signaling Technology) (1:1,000), monoclonal anti-Tubulin Alpha (T6074; Sigma-Aldrich) (1:10,000), anti-mouse secondary antibody (E030110; EarthOx) (1:10,000), and anti-rabbit secondary antibody (E030130; EarthOx) (1:10,000).

IP-MS and coimmunoprecipitation

Synchronized day-1 adult worms grown on plates were collected and washed in M9 buffer. After washing, the animals were resuspended in 0.5 volumes of extraction buffer (50 mM tris-HCl [pH 7.4], 150 mM NaCl, 5 mM dithiothreitol, 10% glycerol, 0.1% NP-40, and protease inhibitors). The suspension was then dripped into liquid N2, and the resulting balls were ground using mortar and pestle. The homogenized worm tissue was resuspended with 2 vol of extraction buffer and lysed at 4°C for 30 min, and the insoluble materials were then removed by centrifugation at 13,000 rpm at 4°C.

For IP-MS, 10 ml of lysate was mixed with GFP-trap agarose (Chromotek) (100 µl) for 4 h and washed five times with wash buffer (50 mM tris-HCl, [pH 7.4], 150 mM NaCl, 10% glycerol, and protease inhibitors). Proteins were eluted using 1% SDS by boiling and then subjected to MS analysis.

The gel-containing sample was decolored in 25 mM ammonium bicarbonate/50% acetonitrile buffer. The proteins in the gel were reduced with 10 mM DTT at 37°C for 1 h and alkylated with 25 mM iodoacetamide at room temperature for 45 min in the dark and digested with trypsin in 25 mM ammonium bicarbonate at 37°C overnight. Peptides were extracted from the gel with a stripping buffer (5% trifluoroacetic acid and 50% acetonitrile) by sonication. The liquid was dried by SpeedVac and the peptides were desalted by StageTips (Rappsilber et al., 2007) before LC-MS/MS analysis.

The samples were analyzed by LTQ Orbitrap Elite mass spectrometer (Thermo Fisher Scientific) coupled online to an Easy-nLC 1000 (Thermo Fisher Scientific) in the data-dependent mode. The peptides were separated by reverse phase LC with a 150 µm (ID) ×250 mm (length) analytical column packed with C18 particles of 1.9 µm diameter with a flow rate of 600 nl/min in a 90-min non-linear gradient. Precursor

ions were measured in the Orbitrap analyzer at 240,000 resolution (at 400 m/z) and a target value of 10^6 ions. The 20 most intense ions from each MS scan were isolated, fragmented, and measured in the linear ion trap. The CID normalized collision energy was set to 35.

The data were analyzed using a pre-release version of Thermo Fisher Scientific Proteome Discoverer software version 1.4. The proteome sequences of *C. elegans* from Uniprot were used for database searching. Cysteine carbamidomethylation was set as the stable modification, and methionine oxidation, lysine acetylation, lysine ubiquitination (GlyGly, 114.043 Da), serine/threonine/tyrosine phosphorylation, and lysine/arginine methylation were included in the search as variable modifications. The protease used for protein digestion was trypsin. The maximum number of missed cleavages was set at two, the minimum peptide length was set at six amino acids, and the maximum peptide length was set at 144 amino acids. The false discovery rate was set at 0.01 for peptide and protein identifications.

See Table S4 for the list of genes identified in the IP-MS experiments. GO analysis of the significant gene list was performed using PANTHER (http://www.pantherdb.org/).

RNA extraction and RT-qPCR

Synchronized L4 stage worms were collected with M9. 1 ml TRIzol (Invitrogen) was added to the tubes which were then snap-frozen in liquid nitrogen. Samples were homogenized by repeated freezing in liquid nitrogen and thawing at 37°C, and total mRNA was then extracted with chloroform treatment, followed by ethanol and isopropanol wash. DNA was wiped off using DNase (RQ1 RNase-Free DNase; Promega). mRNA was extracted again with chloroform treatment, followed by ethanol and isopropanol wash. Amplified cDNA was generated using the M-MLV Reverse Transcriptase kit (Invitrogen). SYBR Green Real-time PCR experiments (SYBR Green Premix Pro Taq HS qPCR Kit; Accurate Biotechnology) were performed using the Real-Time PCR Detection System (Bio-Rad). Relative gene expression was normalized to *act-1(T04C12.6)* mRNA levels (Zhang et al., 2018). A list of the primers is provided in Table S2. Each experiment has been repeated three or more times with biological replicate samples.

Lifespan analysis

Lifespan experiments were conducted on NGM plates at 20°C following a previously established protocol (Dillin et al., 2002). To prevent progeny production, 100 µl 10 mg/ml 5-fluoro-20-deoxyuridine (FUdR) was added to seeded plates. Worms were synchronized by egg bleach and were grown on OP50 from hatching, transitioning to FUdR plates from early adulthood. Worms were scored every second day from day 1 adult stage. Worms were considered dead if they did not respond to gentle touch with the pick and considered censored if missing, having crawled off, burrowed, or carrying internally hatched progeny. All lifespan data are available in the extended data of Table S3. Statistical analysis was performed using Prism 6 software, employing the Log-rank (Mantel-Cox) method to determine the significant difference.

Aversive learning assay

Overnight bacterial cultures were diluted in LB to an optical density (OD_{600}) = 1, and 25 µl of each bacterial suspension was seeded on a 60-mm NGM plate, which was then incubated at 25°C for 2 days. After 2 days, assay plates were left at room temperature for 1 h before use. To initiate the assay (modified from Zhang et al. [2005]), worms were washed off training plates in M9 and then washed two additional times in M9. Approximately, 100–150 synchronized L4 stage worms were spotted at the bottom of the assay plate and then incubated at 25°C for 14–16 h. Assays were photographed to assess the number of worms on each lawn.

Exogenous serotonin supplementation

5-HT hydrochloride powder (Sigma-Aldrich) was dissolved in water to a concentration of 0.1 M as a stock concentration. Then, 100 µl of 50 mM serotonin hydrochloride in water was added on top of an NGM plate with food. Plates were allowed to equilibrate overnight and used the next day (Berendzen et al., 2016; Zhang et al., 2018).

Transcriptome data analysis

To investigate the expression level of *tmbim-2* or *Tmbim2* in *C. elegans*, mice, and humans under aging or disease, we have downloaded the published data from Roux et al. (2023) (*C. elegans*), GSE132040 (mouse), and GSE44772 (human). For *C. elegans*, we downloaded the preprocessed data and subset the *srh-142* positive neurons for Pearson's r correlation coefficient analysis. For mouse data analysis, we extracted transcriptomic data from 17 organs of 3-mo-old mice to investigate region-specific expression patterns of *Tmbim2*. To further identify the correlation between the expression of *Tmbim2* and age, we analyzed the brain, lung, pancreas, and GAT data from mice from 10 to 27 mo of age. We applied quantile normalization to the raw data and log transformed for the values to remove technical variation. Then we calculated Pearson's r correlation coefficient for statistical testing. For human data analysis, preprocessed microarray data were downloaded with series normalization as previously reported (Schaum et al., 2020). Prefrontal cortex samples with Alzheimer's disease were subset to perform Pearson's r correlation coefficient for statistical testing. The results were visualized using the ggplot2 (v.3.3.5) and ggpubr (v.0.4) R package (https://github.com/kassambara/ggpubr).

Statistical analysis

Experimental data were analyzed using GraphPad Prism (v.6.01). For all graphs, the error bars indicate the mean ± SEM. Differences were significant when $P < 0.05$. Statistical significance is indicated by asterisks; *$P < 0.05$; **$P < 0.01$; ***$P < 0.001$. *n* represents the number of biological replicates unless otherwise indicated. No data were excluded from the analyses. To compare two normally distributed groups, two-tailed *t* tests were used. For comparisons between multiple groups with one fixed factor, an ordinary one-way ANOVA or one-way repeated-measures ANOVA was used, followed by Dunnett's multiple-comparisons test or Tukey's multiple-comparisons

test. Lifespans and slow-killing assays were analyzed using the Mantel–Cox log-rank test. All experiments were performed at least three times yielding similar results and comprised of biological replicates. All data points for all replicates for specific quantifications are provided in the source data.

Online supplemental material

Fig. S1 shows the XBX-6/TMBIM-2 functions in neurons to coordinate neuronal-to-intestinal UPR^{mt} activation. Fig. S2 shows the expression and subcellular distribution of TMBIM-2 in response to neuronal mitochondrial stress. Fig. S3 indicates that mitochondrial perturbation does not affect the dynamics of cytosol Ca^{2+} waves in ADF synapses. Fig. S4 shows the activation of the UPR^{mt} upon overexpression of MCU-1 or loss of *mca-3* in neurons. Fig. S5 shows the systemic UPR^{mt} activation in *tmbim-2* mutants after supplementing serotonin. Table S1 contains information on *C. elegans* strains. Table S2 shows the list of primers in this study. Table S3 shows the lifespan date in this study. Table S4 shows the list of genes identified in the IP-MS experiments. Video 1 depicts the plasma-membrane Ca^{2+} oscillations within the synapse of ADF neurons with mitochondrial perturbation.

Data availability

All data related to this paper may be requested from the corresponding author. All strains synthesized in this manuscript are derivatives of N2 or other strains from CGC and are made available upon request.

Acknowledgments

We thank Tian lab members for assistance with strain maintenance and reporter crosses; Dr. S. Xu and Dr. J.F. Liu for providing the GCaMP6f and TeTx plasmids; Dr. L.J. Kang and Dr. S.B. Gao for calcium imaging; L. Wang and X.X. Li prepared the EM samples and took EM images; Y. Feng, Q. Bian, and C.L. Liu helped with taking confocal images and analyzing the results. Our LSM980 confocal microscopy work was performed at the Bio-imaging Facility, Institute of Genetics and Developmental Biology, Chinese Academy of Science. We thank Dr. M. Ding, Dr. X. Huang, Dr. Y.L. Li, and Dr. Z.F. Wu for the discussion and suggestions. We thank Dr. Y. Fu, Dr. W.X. Meng, and Dr. F.P. Zhu for their technical support.

This work was supported by the National Key R&D Program of China (2022YFA1303000 to Y. Tian and 2019YFA0800213 to Q. Wu), the Strategic Priority Research Program of the Chinese Academy of Sciences (XDB39000000 to Y. Tian), and the National Natural Science Foundation of China (32430025, 31930023, 32225025, 92254305, 32321004 to Y. Tian and 32230031, 81891002 to Q. Wu), and the CAS Project for Young Scientists in Basic Research (YSBR-076 to Y. Tian). Beijing Municipal Science & Technology Commission (Z210010 to Q. Wu). The New Cornerstone Science Foundation supports Y. Tian through the XPLORER PRIZE. Several *C. elegans* strains used in this work were provided by the *Caenorhabditis Genetics Center* (CGC), which is supported by the NIH-Officer of Research Infrastructure Programs (P40 OD010440).

Author contributions: J. Li: Conceptualization, Data curation, Formal analysis, Methodology, Validation, Writing - original draft, J. Cui: Investigation, X. Li: Data curation, Formal analysis, Investigation, Validation, Visualization, D. Zhu: Investigation, Methodology, Resources, Z. Chen: Data curation, Validation, X. Huang: Formal analysis, Y. Wang: Investigation, Q. Wu: Methodology, Y. Tian: Conceptualization, Funding acquisition, Project administration, Supervision, Writing - review & editing.

Disclosures: The authors declare no competing interests exist.

Submitted: 11 August 2024
Revised: 11 December 2024
Accepted: 9 February 2025

References

Anderson, N.S., and C.M. Haynes. 2020. Folding the mitochondrial UPR into the integrated stress response. *Trends Cell Biol.* 30:428–439. https://doi.org/10.1016/j.tcb.2020.03.001

Bar-Ziv, R., T. Bolas, and A. Dillin. 2020. Systemic effects of mitochondrial stress. *EMBO Rep.* 21:e50094. https://doi.org/10.15252/embr.202050094

Berendzen, K.M., J. Durieux, L.W. Shao, Y. Tian, H.E. Kim, S. Wolff, Y. Liu, and A. Dillin. 2016. Neuroendocrine coordination of mitochondrial stress signaling and proteostasis. *Cell.* 166:1553–1563.e10. https://doi.org/10.1016/j.cell.2016.08.042

Berliocchi, L., D. Bano, and P. Nicotera. 2005. Ca^{2+} signals and death programmes in neurons. *Philos. Trans. R. Soc. Lond. B Biol. Sci.* 360:2255–2258. https://doi.org/10.1098/rstb.2005.1765

Berridge, M.J., M.D. Bootman, and H.L. Roderick. 2003. Calcium signalling: Dynamics, homeostasis and remodelling. *Nat. Rev. Mol. Cell Biol.* 4:517–529. https://doi.org/10.1038/nrm1155

Berridge, M.J., P. Lipp, and M.D. Bootman. 2000. The versatility and universality of calcium signalling. *Nat. Rev. Mol. Cell Biol.* 1:11–21. https://doi.org/10.1038/35036035

Brenner, S. 1974. The genetics of Caenorhabditis elegans. *Genetics.* 77:71–94. https://doi.org/10.1093/genetics/77.1.71

Brini, M., and E. Carafoli. 2011. The plasma membrane Ca^{2+} ATPase and the plasma membrane sodium calcium exchanger cooperate in the regulation of cell calcium. *Cold Spring Harb. Perspect. Biol.* 3:a004168. https://doi.org/10.1101/cshperspect.a004168

Bultynck, G., S. Kiviluoto, N. Henke, H. Ivanova, L. Schneider, V. Rybalchenko, T. Luyten, K. Nuyts, W. De Borggraeve, I. Bezprozvanny, et al. 2012. The C terminus of Bax inhibitor-1 forms a Ca^{2+}-permeable channel pore. *J. Biol. Chem.* 287:2544–2557. https://doi.org/10.1074/jbc.M111.275354

Cai, H., W.N. Cong, S. Ji, S. Rothman, S. Maudsley, and B. Martin. 2012. Metabolic dysfunction in Alzheimer's disease and related neurodegenerative disorders. *Curr. Alzheimer Res.* 9:5–17. https://doi.org/10.2174/156720512799015064

Cao, C., S. Wang, T. Cui, X.C. Su, and J.J. Chou. 2017. Ion and inhibitor binding of the double-ring ion selectivity filter of the mitochondrial calcium uniporter. *Proc. Natl. Acad. Sci. USA.* 114:E2846–E2851. https://doi.org/10.1073/pnas.1620316114

Carafoli, E., L. Santella, D. Branca, and M. Brini. 2001. Generation, control, and processing of cellular calcium signals. *Crit. Rev. Biochem. Mol. Biol.* 36:107–260. https://doi.org/10.1080/20014091074183

Carter, R. 2019. The Human Brain Book: An Illustrated Guide to Its Structure, Function, and Disorders. Penguin, New York, NY, USA. 264 pp.

Chang, Y., R. Bruni, B. Kloss, Z. Assur, E. Kloppmann, B. Rost, W.A. Hendrickson, and Q. Liu. 2014. Structural basis for a pH-sensitive calcium leak across membranes. *Science.* 344:1131–1135. https://doi.org/10.1126/science.1252043

Chaudhary, J., M. Walia, J. Matharu, E. Escher, and A.K. Grover. 2001. Calcoxin: A novel plasma membrane Ca^{2+} pump inhibitor. *Am. J. Physiol. Cell Physiol.* 280:C1027–C1030. https://doi.org/10.1152/ajpcell.2001.280.4.C1027

Chen, L.T., C.T. Lin, L.Y. Lin, J.M. Hsu, Y.C. Wu, and C.L. Pan. 2021. Neuronal mitochondrial dynamics coordinate systemic mitochondrial morphology

and stress response to confer pathogen resistance in C. elegans. *Dev. Cell.* 56:1770–1785.e12. https://doi.org/10.1016/j.devcel.2021.04.021

Chen, T.W., T.J. Wardill, Y. Sun, S.R. Pulver, S.L. Renninger, A. Baohan, E.R. Schreiter, R.A. Kerr, M.B. Orger, V. Jayaraman, et al. 2013. Ultrasensitive fluorescent proteins for imaging neuronal activity. *Nature.* 499: 295–300. https://doi.org/10.1038/nature12354

Chung, S.H., L. Sun, and C.V. Gabel. 2013. In vivo neuronal calcium imaging in C. elegans. *J. Vis. Exp.* 50357. https://doi.org/10.3791/50357

Davis, M.W., M. Hammarlund, T. Harrach, P. Hullett, S. Olsen, and E.M. Jorgensen. 2005. Rapid single nucleotide polymorphism mapping in C. elegans. *BMC Genomics.* 6:118. https://doi.org/10.1186/1471-2164-6-118

Devine, M.J., and J.T. Kittler. 2018. Mitochondria at the neuronal presynapse in health and disease. *Nat. Rev. Neurosci.* 19:63–80. https://doi.org/10.1038/nrn.2017.170

Dillin, A., A.L. Hsu, N. Arantes-Oliveira, J. Lehrer-Graiwer, H. Hsin, A.G. Fraser, R.S. Kamath, J. Ahringer, and C. Kenyon. 2002. Rates of behavior and aging specified by mitochondrial function during development. *Science.* 298:2398–2401. https://doi.org/10.1126/science.1077780

Doser, R.L., K.M. Knight, E.W. Deihl, and F.J. Hoerndli. 2024. Activity-dependent mitochondrial ROS signaling regulates recruitment of glutamate receptors to synapses. *Elife.* 13:e92376. https://doi.org/10.7554/eLife.92376

Duarte, J.M., P.F. Schuck, G.L. Wenk, and G.C. Ferreira. 2013. Metabolic disturbances in diseases with neurological involvement. *Aging Dis.* 5: 238–255. https://doi.org/10.14336/AD.2014.0500238

Durieux, J., S. Wolff, and A. Dillin. 2011. The cell-non-autonomous nature of electron transport chain-mediated longevity. *Cell.* 144:79–91. https://doi.org/10.1016/j.cell.2010.12.016

Gherardi, G., H. Monticelli, R. Rizzuto, and C. Mammucari. 2020. The mitochondrial Ca^{2+} uptake and the fine-tuning of aerobic metabolism. *Front. Physiol.* 11:554904. https://doi.org/10.3389/fphys.2020.554904

Giacomello, M., A. Pyakurel, C. Glytsou, and L. Scorrano. 2020. The cell biology of mitochondrial membrane dynamics. *Nat. Rev. Mol. Cell Biol.* 21: 204–224. https://doi.org/10.1038/s41580-020-0210-7

Giorgi, C., S. Marchi, and P. Pinton. 2018. The machineries, regulation and cellular functions of mitochondrial calcium. *Nat. Rev. Mol. Cell Biol.* 19: 713–730. https://doi.org/10.1038/s41580-018-0052-8

Guo, Y., D. Li, S. Zhang, Y. Yang, J.J. Liu, X. Wang, C. Liu, D.E. Milkie, R.P. Moore, U.S. Tulu, et al. 2018. Visualizing intracellular organelle and cytoskeletal interactions at nanoscale resolution on millisecond timescales. *Cell.* 175:1430–1442.e17. https://doi.org/10.1016/j.cell.2018.09.057

Han, M., W. Zou, H. Chang, Y. Yu, H. Zhang, S. Li, H. Cheng, G. Wei, Y. Chen, V. Reinke, et al. 2017. A systematic RNAi screen reveals a novel role of a spindle assembly checkpoint protein BuGZ in synaptic transmission in *C. elegans*. *Front. Mol. Neurosci.* 10:141. https://doi.org/10.3389/fnmol.2017.00141

Hendricks, M., H. Ha, N. Maffey, and Y. Zhang. 2012. Compartmentalized calcium dynamics in a C. elegans interneuron encode head movement. *Nature.* 487:99–103. https://doi.org/10.1038/nature11081

Holmes, M.E., J. Chaudhary, and A.K. Grover. 2003. Mechanism of action of the novel plasma membrane Ca(2+)-pump inhibitor caloxin. *Cell Calcium.* 33:241–245. https://doi.org/10.1016/S0143-4160(02)00207-5

Kwon, S.K., R. Sando III, T.L. Lewis, Y. Hirabayashi, A. Maximov, and F. Polleux. 2016. LKB1 regulates mitochondria-dependent presynaptic calcium clearance and neurotransmitter release properties at excitatory synapses along cortical axons. *PLoS Biol.* 14:e1002516. https://doi.org/10.1371/journal.pbio.1002516

Labbadia, J., and R.I. Morimoto. 2015. The biology of proteostasis in aging and disease. *Annu. Rev. Biochem.* 84:435–464. https://doi.org/10.1146/annurev-biochem-060614-033955

Levy, M., G.C. Faas, P. Saggau, W.J. Craigen, and J.D. Sweatt. 2003. Mitochondrial regulation of synaptic plasticity in the hippocampus. *J. Biol. Chem.* 278:17727–17734. https://doi.org/10.1074/jbc.M212878200

Li, C.C., T.Y. Kao, C.C. Cheng, and Y.W. Chiang. 2020a. Structure and regulation of the BsYetJ calcium channel in lipid nanodiscs. *Proc. Natl. Acad. Sci. USA.* 117:30126–30134. https://doi.org/10.1073/pnas.2014094117

Li, S., and Z.H. Sheng. 2022. Energy matters: Presynaptic metabolism and the maintenance of synaptic transmission. *Nat. Rev. Neurosci.* 23:4–22. https://doi.org/10.1038/s41583-021-00535-8

Li, S., G.J. Xiong, N. Huang, and Z.H. Sheng. 2020b. The cross-talk of energy sensing and mitochondrial anchoring sustains synaptic efficacy by maintaining presynaptic metabolism. *Nat. Metab.* 2:1077–1095. https://doi.org/10.1038/s42255-020-00289-0

Li, T.Y., A.W. Gao, X. Li, H. Li, Y.J. Liu, A. Lalou, N. Neelagandan, F. Naef, K. Schoonjans, and J. Auwerx. 2023. V-ATPase/TORC1-mediated ATFS-1 translation directs mitochondrial UPR activation in C. elegans. *J. Cell Biol.* 222:e202205045. https://doi.org/10.1083/jcb.202205045

Li, X., J. Li, D. Zhu, N. Zhang, X. Hao, W. Zhang, Q. Zhang, Y. Liu, X. Wu, and Y. Tian. 2022. Protein disulfide isomerase PDI-6 regulates Wnt secretion to coordinate inter-tissue UPR^{mt} activation and lifespan extension in C. elegans. *Cell Rep.* 39:110931. https://doi.org/10.1016/j.celrep.2022.110931

Liu, Q. 2017. TMBIM-mediated Ca^{2+} homeostasis and cell death. *Biochim. Biophys. Acta Mol. Cell Res.* 1864:850–857. https://doi.org/10.1016/j.bbamcr.2016.12.023

Liu, Y., J. Zhou, N. Zhang, X. Wu, Q. Zhang, W. Zhang, X. Li, and Y. Tian. 2022. Two sensory neurons coordinate the systemic mitochondrial stress response via GPCR signaling in C. elegans. *Dev. Cell.* 57: 2469–2482.e5. https://doi.org/10.1016/j.devcel.2022.10.001

Marland, J.R., P. Hasel, K. Bonnycastle, and M.A. Cousin. 2016. Mitochondrial calcium uptake modulates synaptic vesicle endocytosis in central nerve terminals. *J. Biol. Chem.* 291:2080–2086. https://doi.org/10.1074/jbc.M115.686956

Mashal, R.D., J. Koontz, and J. Sklar. 1995. Detection of mutations by cleavage of DNA heteroduplexes with bacteriophage resolvases. *Nat. Genet.* 9: 177–183. https://doi.org/10.1038/ng0295-177

Mills, H., A. Ortega, W. Law, V. Hapiak, P. Summers, T. Clark, and R. Komuniecki. 2016. Opiates modulate noxious chemical nociception through a complex monoaminergic/peptidergic cascade. *J. Neurosci.* 36: 5498–5508. https://doi.org/10.1523/JNEUROSCI.4520-15.2016

Monzel, A.S., J.A. Enríquez, and M. Picard. 2023. Multifaceted mitochondria: Moving mitochondrial science beyond function and dysfunction. *Nat. Metab.* 5:546–562. https://doi.org/10.1038/s42255-023-00783-1

Nanou, E., and W.A. Catterall. 2018. Calcium channels, synaptic plasticity, and neuropsychiatric disease. *Neuron.* 98:466–481. https://doi.org/10.1016/j.neuron.2018.03.017

Orrenius, S., B. Zhivotovsky, and P. Nicotera. 2003. Regulation of cell death: The calcium-apoptosis link. *Nat. Rev. Mol. Cell Biol.* 4:552–565. https://doi.org/10.1038/nrm1150

Pande, J., K.K. Mallhi, and A.K. Grover. 2005. A novel plasma membrane Ca^{2+}-pump inhibitor: Caloxin 1A1. *Eur. J. Pharmacol.* 508:1–6. https://doi.org/10.1016/j.ejphar.2004.11.057

Pande, J., M.M. Szewczyk, I. Kuszczak, S. Grover, E. Escher, and A.K. Grover. 2008. Functional effects of caloxin 1c2, a novel engineered selective inhibitor of plasma membrane Ca^{2+}-pump isoform 4, on coronary artery. *J. Cell. Mol. Med.* 12:1049–1060. https://doi.org/10.1111/j.1582-4934.2008.00140.x

Pang, Z.P., and T.C. Südhof. 2010. Cell biology of Ca^{2+}-triggered exocytosis. *Curr. Opin. Cell Biol.* 22:496–505. https://doi.org/10.1016/j.ceb.2010.05.001

Phillips, C.B., C.W. Tsai, and M.F. Tsai. 2019. The conserved aspartate ring of MCU mediates MICU1 binding and regulation in the mitochondrial calcium uniporter complex. *Elife.* 8:e41112. https://doi.org/10.7554/eLife.41112

Rappsilber, J., M. Mann, and Y. Ishihama. 2007. Protocol for micro-purification, enrichment, pre-fractionation and storage of peptides for proteomics using StageTips. *Nat. Protoc.* 2:1896–1906. https://doi.org/10.1038/nprot.2007.261

Reich, A., C. Spering, K. Gertz, C. Harms, E. Gerhardt, G. Kronenberg, K.A. Nave, M. Schwab, S.C. Tauber, A. Drinkut, et al. 2011. Fas/CD95 regulatory protein Faim2 is neuroprotective after transient brain ischemia. *J. Neurosci.* 31:225–233. https://doi.org/10.1523/JNEUROSCI.2188-10.2011

Rojas-Rivera, D., and C. Hetz. 2015. TMBIM protein family: Ancestral regulators of cell death. *Oncogene.* 34:269–280. https://doi.org/10.1038/onc.2014.6

Roux, A.E., H. Yuan, K. Podshivalova, D. Hendrickson, R. Kerr, C. Kenyon, and D. Kelley. 2023. Individual cell types in C. elegans age differently and activate distinct cell-protective responses. *Cell Rep.* 42:112902. https://doi.org/10.1016/j.celrep.2023.112902

Schaum, N., B. Lehallier, O. Hahn, R. Pálovics, S. Hosseinzadeh, S.E. Lee, R. Sit, D.P. Lee, P.M. Losada, M.E. Zardeneta, et al. 2020. Ageing hallmarks exhibit organ-specific temporal signatures. *Nature.* 583:596–602. https://doi.org/10.1038/s41586-020-2499-y

Schweitzer, B., U. Suter, and V. Taylor. 2002. Neural membrane protein 35/Lifeguard is localized at postsynaptic sites and in dendrites. *Brain Res. Mol. Brain Res.* 107:47–56. https://doi.org/10.1016/S0169-328X(02)00445-X

Shao, L.W., R. Niu, and Y. Liu. 2016. Neuropeptide signals cell non-autonomous mitochondrial unfolded protein response. *Cell Res.* 26: 1182–1196. https://doi.org/10.1038/cr.2016.118

Shen, E.Z., C.Q. Song, Y. Lin, W.H. Zhang, P.F. Su, W.Y. Liu, P. Zhang, J. Xu, N. Lin, C. Zhan, et al. 2014. Mitoflash frequency in early adulthood predicts lifespan in Caenorhabditis elegans. *Nature*. 508:128–132. https://doi.org/10.1038/nature13012

Shpilka, T., and C.M. Haynes. 2018. The mitochondrial UPR: Mechanisms, physiological functions and implications in ageing. *Nat. Rev. Mol. Cell Biol.* 19:109–120. https://doi.org/10.1038/nrm.2017.110

Südhof, T.C. 2018. Towards an understanding of synapse formation. *Neuron*. 100:276–293. https://doi.org/10.1016/j.neuron.2018.09.040

Sze, J.Y., M. Victor, C. Loer, Y. Shi, and G. Ruvkun. 2000. Food and metabolic signalling defects in a Caenorhabditis elegans serotonin-synthesis mutant. *Nature*. 403:560–564. https://doi.org/10.1038/35000609

Szewczyk, M.M., J. Pande, G. Akolkar, and A.K. Grover. 2010. Caloxin 1b3: A novel plasma membrane Ca(2+)-pump isoform 1 selective inhibitor that increases cytosolic Ca(2+) in endothelial cells. *Cell Calcium*. 48:352–357. https://doi.org/10.1016/j.ceca.2010.10.008

Tang, Y., and R.S. Zucker. 1997. Mitochondrial involvement in post-tetanic potentiation of synaptic transmission. *Neuron*. 18:483–491. https://doi.org/10.1016/S0896-6273(00)81248-9

Tauber, S.C., K. Harms, B. Falkenburger, J. Weis, B. Sellhaus, R. Nau, J.B. Schulz, and A. Reich. 2014. Modulation of hippocampal neuroplasticity by Fas/CD95 regulatory protein 2 (Faim2) in the course of bacterial meningitis. *J. Neuropathol. Exp. Neurol.* 73:2–13. https://doi.org/10.1097/NEN.0000000000000020

van der Kolk, B.A. 2006. Clinical implications of neuroscience research in PTSD. *Ann. N. Y. Acad. Sci.* 1071:277–293. https://doi.org/10.1196/annals.1364.022

van Oosten-Hawle, P., and R.I. Morimoto. 2014. Organismal proteostasis: Role of cell-nonautonomous regulation and transcellular chaperone signaling. *Genes Dev.* 28:1533–1543. https://doi.org/10.1101/gad.241125.114

Waaijers, S., V. Portegijs, J. Kerver, B.B. Lemmens, M. Tijsterman, S. van den Heuvel, and M. Boxem. 2013. CRISPR/Cas9-targeted mutagenesis in Caenorhabditis elegans. *Genetics*. 195:1187–1191. https://doi.org/10.1534/genetics.113.156299

Wang, Z., Q. Zhang, Y. Jiang, J. Zhou, and Y. Tian. 2024. ASI-RIM neuronal axis regulates systemic mitochondrial stress response via TGF-β signaling cascade. *Nat. Commun.* 15:8997. https://doi.org/10.1038/s41467-024-53093-9

Zhang, B., C. Gaiteri, L.G. Bodea, Z. Wang, J. McElwee, A.A. Podtelezhnikov, C. Zhang, T. Xie, L. Tran, R. Dobrin, et al. 2013. Integrated systems approach identifies genetic nodes and networks in late-onset Alzheimer's disease. *Cell*. 153:707–720. https://doi.org/10.1016/j.cell.2013.03.030

Zhang, B., H. Jun, J. Wu, J. Liu, and X.Z.S. Xu. 2021a. Olfactory perception of food abundance regulates dietary restriction-mediated longevity via a brain-to-gut signal. *Nat. Aging*. 1:255–268. https://doi.org/10.1038/s43587-021-00039-1

Zhang, Q., Z. Wang, W. Zhang, Q. Wen, X. Li, J. Zhou, X. Wu, Y. Guo, Y. Liu, C. Wei, et al. 2021b. The memory of neuronal mitochondrial stress is inherited transgenerationally via elevated mitochondrial DNA levels. *Nat. Cell Biol.* 23:870–880. https://doi.org/10.1038/s41556-021-00724-8

Zhang, Q., X. Wu, P. Chen, L. Liu, N. Xin, Y. Tian, and A. Dillin. 2018. The mitochondrial unfolded protein response is mediated cell-non-autonomously by retromer-dependent Wnt signaling. *Cell*. 174:870–883.e17. https://doi.org/10.1016/j.cell.2018.06.029

Zhang, Y., H. Lu, and C.I. Bargmann. 2005. Pathogenic bacteria induce aversive olfactory learning in Caenorhabditis elegans. *Nature*. 438: 179–184. https://doi.org/10.1038/nature04216

Zheng, Q., Y. Chen, D. Chen, H. Zhao, Y. Feng, Q. Meng, Y. Zhao, and H. Zhang. 2022. Calcium transients on the ER surface trigger liquid-liquid phase separation of FIP200 to specify autophagosome initiation sites. *Cell*. 185:4082–4098.e22. https://doi.org/10.1016/j.cell.2022.09.001

Zhou, K., S.J. Cherra III, A. Goncharov, and Y. Jin. 2017. Asynchronous cholinergic drive correlates with excitation-inhibition imbalance via a neuronal Ca^{2+} sensor protein. *Cell Rep.* 19:1117–1129. https://doi.org/10.1016/j.celrep.2017.04.043

Zhu, D., X. Li, and Y. Tian. 2022. Mitochondrial-to-nuclear communication in aging: An epigenetic perspective. *Trends Biochem. Sci.* 47:645–659. https://doi.org/10.1016/j.tibs.2022.03.008

JCB

Supplemental material

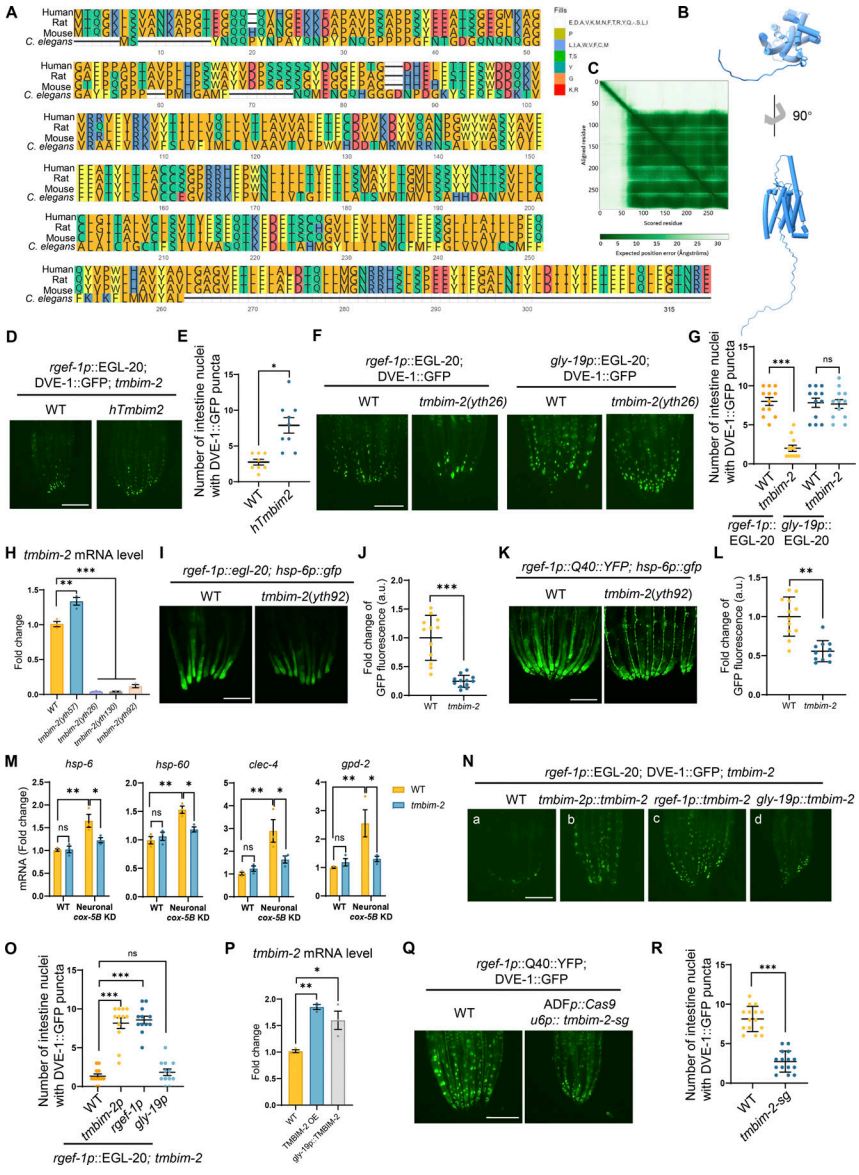

Figure S1. **XBX-6/TMBIM-2 functions in neurons to coordinate neuronal-to-intestinal UPR^{mt} activation. (A)** Sequence alignment of TMBIM2 proteins across species. **(B)** Alphafold predicted the protein structure of TMBIM-2. **(C)** A PAE (Predicted Aligned Error) plot, showing regions of high confidence (dark green) and low confidence (pale green) for the AlphaFold prediction of TMBIM-2 structure. **(D)** Representative photomicrograph of *dve-1* reporter in neuronal EGL-20; *tmbim-2* animals with or without human TMBIM2 overexpressing (*tmbim-2p::hTmbim2)* rescue. **(E)** Quantification of the number of intestinal nuclei puncta with GFP signal per worm as shown in D. $n \geq 9$ biologically independent samples. **(F)** Representative photomicrographs of *dve-1* reporter expression in neuronal EGL-20 overexpressing (*ythIs3[rgef-1p::egl-20 + myo-2p::tdtomato]*) and intestinal EGL-20 overexpressing (*ythIs1[gly-19p::egl-20]*) animals in WT or *tmbim-2(yth26)* background, respectively. The posterior region of the intestine where DVE-1::GFP is induced or suppressed is highlighted. **(G)** Quantification of the number of intestinal nuclei puncta with GFP signal per worm as shown in F. $n \geq 12$ worms. **(H)** Quantification of *tmbim-2* mRNA levels in WT (yellow), *tmbim-2 (yth57)* (blue), *tmbim-2 (yth26)* (purple), *tmbim-2 (yth130)* (grey), and *tmbim-2 (yth92)* (pink) animals. Error bars, SEM; $n \geq 3$ biologically independent samples. **(I)** Representative photomicrographs of *hsp-6* reporter (*zcIs3[hsp-6p::gfp]*) expression in neuronal EGL-20 overexpressing (*ythIs3[rgef-1p::egl-20 + myo-2p::tdtomato]*) animals in WT or *tmbim-2(yth92)* background, respectively. **(J)** Quantification of *hsp-6p::gfp* expression in the entire intestine of animals as depicted in I. $n \geq 15$ worms. **(K)** Representative photomicrographs of *hsp-6* reporter (*zcIs3[hsp-6p::gfp]*) expression in neuronal Q40::YFP overexpressing animals in WT or *tmbim-2(yth92)* background, respectively. **(L)** Quantification of *hsp-6p::gfp* expression. The genotypes are as in K. $n \geq 15$ worms. **(M)** qRT-PCR analysis of transcripts ($n = 3$ biologically independent samples) in neuronal *cox-5B* knockdown animals in WT or *tmbim-2* background. Statistical analysis was performed by ANOVA followed by Tukey post-hoc test (**P < 0.01; *P < 0.05). **(N)** Representative photomicrographs demonstrating: *dve-1* reporter expression in *tmbim-2 (yth57)* animals expressing neuronal EGL-20 **(a)**; TMBIM-2 rescue (*ythIs62[tmbim-2p::tmbim-2::GFP; unc-119(+)]*) **(b)**; TMBIM-2 pan-neuron rescue (*ythEx226 [rgef-1p::tmbim-2::mcherry::HA; pRF4(rol-6)]*) **(c)**; TMBIM-2 intestinal rescue (*ythEx229[gly-19p::tmbim-2::mcherry::HA; pRF4(rol-6)]*) **(d)**. The posterior region of the intestine where DVE-1::GFP is induced or suppressed is highlighted. **(O)** Quantification of the number of intestinal nuclei puncta with GFP signal per worm as shown in N. **(P)** Quantification of *tmbim-2* mRNA levels in WT, TMBIM-2 overexpression and intestinal TMBIM-2 overexpression animals. Error bars, SEM; $n \geq 3$ biologically independent samples. **(Q)** Representative photomicrograph of *dve-1* reporter in neuronal Q40::YFP overexpressing animals with or without ADF neuronal TMBIM-2 knockout (*ythEx574[srh-142p::Cas9::u6p::tmbim-2 sgRNA]*). **(R)** Quantification of the number of intestinal nuclei puncta with GFP signal per worm as shown in Q. $n \geq 15$ worms. ***P < 0.001, *P < 0.05, ns denotes P > 0.05 via unpaired two-tailed Student's *t* test. Error bars, SEM. Scale bar, 250 µm.

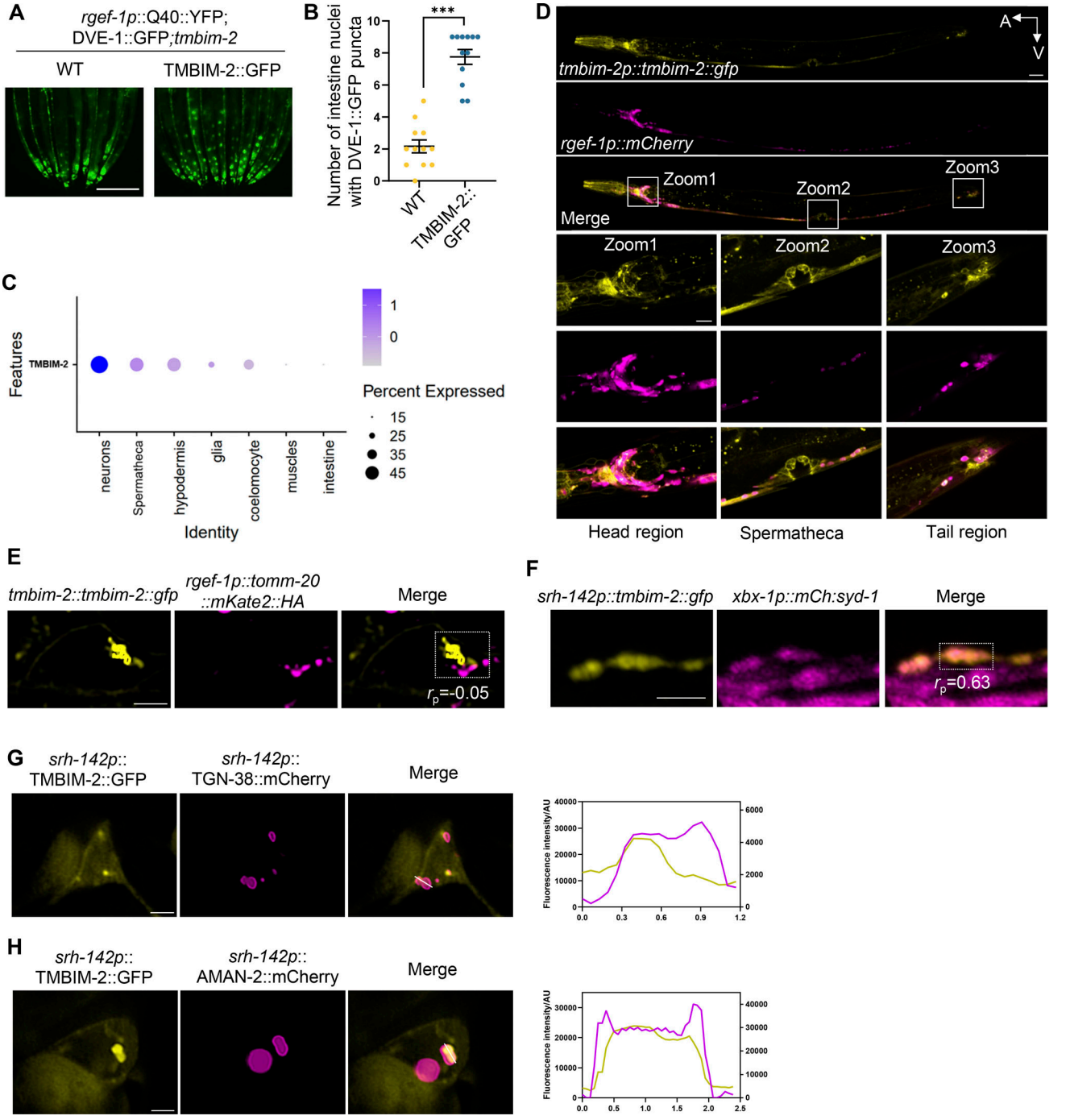

Figure S2. **The expression and subcellular distribution of TMBIM-2 in response to neuronal mitochondrial stress. (A)** Representative photomicrograph of *dve-1* reporter in *tmbim-2(yth57)*; neuronal Q40 overexpressing animals with or without TMBIM-2::GFP rescue. Scale bar, 250 µm. **(B)** Quantification of the number of intestinal nuclei puncta with GFP signal per worm as shown in A. $n \geq 12$ worms. **(C)** The Dot plot shows the average expression of TMBIM-2 in kinds of *C. elegans* tissues. Expression values are from Roux et al. (2023). **(D)** Representative confocal photomicrographs of day 1 adult animals with *ythIs62[tmbim-2p::tmbim-2::gfp]* in combination with a pan-neuron marker *rgef-1p::mcherry*. Scale bar, 20 µm. Panels below show high-magnification views of boxed regions Zoom 1 (Head region), Zoom 2 (Spermatheca), and Zoom 3 (Tail region). The imaging used Z-planes. Scale bar, 5 µm. **(E)** Representative confocal photomicrographs of day 1 adult animals with *ythIs62[tmbim-2p::tmbim-2::gfp]* in combination with a neuronal mitochondria marker (*forSi44[rgef-1p::tomm-20::mKate2::HA]*). The imaging used Z-planes. Scale bar, 2 µm. Pearson's correlation coefficient (r) for the ROI is −0.05. **(F)** Representative confocal photomicrographs of day 1 adult animals with *ythIs62[tmbim-2p::tmbim-2::gfp]* in combination with the synaptic active zone marker (*ythEX774[xbx-1p::mcherry::syd-1]*). The imaging used Z-planes. Scale bar, 2 µm. Pearson's correlation coefficient (r) for the ROI is 0.63. **(G)** Representative confocal photomicrographs of day 1 adult animals with ADF neuron overexpressing TMBIM-2 (*ythIs102[srh-142p::tmbim-2]*) in combination with the trans-Golgi marker (TGN-38::mCherry). The imaging used Z-planes. Scale bar, 2 µm. **(H)** Representative confocal photomicrographs of day 1 adult animals with ADF neuron overexpressing TMBIM-2 (*ythIs102[srh-142p::tmbim-2]*) in combination with the medial/cis-Golgi marker (AMAN-2::mCherry). The imaging used Z-planes. Scale bar, 2 µm. ***P < 0.001 via unpaired two-tailed Student's *t* test. Error bars, SEM.

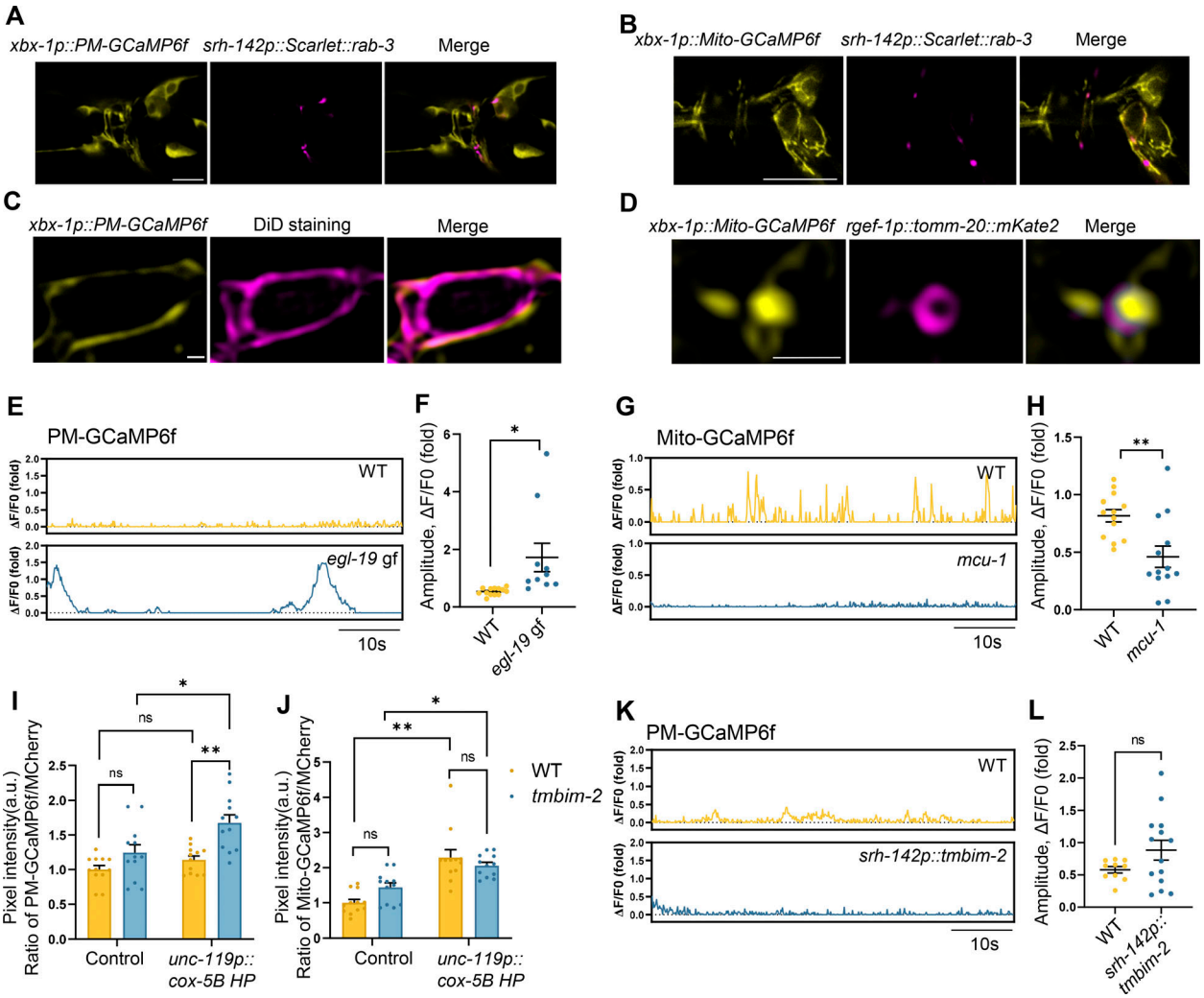

Figure S3. **Mitochondrial perturbation does not affect the dynamics of cytosol Ca^{2+} waves in ADF synapses. (A)** Representative confocal photomicrographs of day 1 adult animals expressing neuronal PM-GCaMP6f in combination with ADF presynaptic vesicle marker *(ythEX762[xbx-1p::PM-GCaMP6f; srh-142p:: Scarlet::rab-3+unc-119(+)])*. The imaging used Z-planes. Scale bar, 10 µm. **(B)** Representative confocal photomicrographs of day 1 adult animals expressing neuronal mito-GCaMP6f in combination with ADF presynaptic vesicle marker *(ythEX761[xbx-1p::mtLS-GCaMP6f; srh-142p:: Scarlet::rab-3+unc-119(+)])*. The imaging used Z-planes. Scale bar, 10 µm. **(C)** Representative confocal photomicrographs of day 1 adult animals expressing neuronal PM-GCaMP6f with plasma membrane dye DiD. The imaging used Z-planes. Scale bar, 1 µm. **(D)** Representative confocal photomicrographs of day 1 adult animals expressing neuronal mito-GCaMP6f in combination with neuronal mitochondria marker *(forSi44[rgef-1p::tomm-20::mKate2::HA])*. Scale bar, 1 µm. The imaging used Z-planes. Scale bar, 1 µm. **(E)** Representative fluorescence traces of average background-subtracted fluorescence intensity ΔF/F0 of plasma membrane Ca^{2+} indicator GCaMP6f of WT and *egl-19(ad695)* gain of function mutant animals in the 60 s. **(F)** Quantification of the amplitude of PM-GCaMP6f fluorescence intensity changes in WT and *egl-19(ad695)* animals. $n \geq 10$ worms. **(G)** Representative fluorescence traces of average background-subtracted fluorescence intensity ΔF/F0 of mitochondrial Ca^{2+} indicator GCaMP6f of WT and *mcu-1(ju1154)* mutant animals in the 60 s. **(H)** Quantification of the amplitude of mito-GCaMP6f fluorescence intensity changes in WT and *mcu-1(ju1154)* animals. $n \geq 13$ worms. **(I)** Quantitative analysis of Ca^{2+} F_{min} level by the PM-GCaMP6.0/RFP ratio with the presence or absence of neuronal *cox-5B* KD in WT (yellow) *and tmbim-2* (blue) animals. $n \geq 12$ worms. **(J)** Quantitative analysis of Ca^{2+} F_{min} level by the Mito-GCaMP6.0/RFP ratio with the presence or absence of neuronal *cox-5B* KD in WT (yellow) *and tmbim-2* (blue) animals. $n \geq 12$ worms. **(K)** Representative fluorescence traces of average background-subtracted fluorescence intensity ΔF/F0 of plasma membrane Ca^{2+} indicator GCaMP6f of WT and ADF neuron overexpressing TMBIM-2 (*ythIs102[srh-142p::tmbim-2]*) animals in 60 s. **(L)** Quantification of the amplitude of PM-GCaMP6f fluorescence intensity changes in WT and ADF neuron overexpressing TMBIM-2 animals. $n \geq 14$ worms. $^{**}P < 0.01$; $^{*}P < 0.05$; ns denotes $P > 0.05$ via unpaired two-tailed Student's *t* test in F, H, and L. Statistical analysis was performed by ANOVA followed by Tukey post-hoc test in I and J ($^{**}P < 0.01$; $^{***}P < 0.001$). Error bars, SEM.

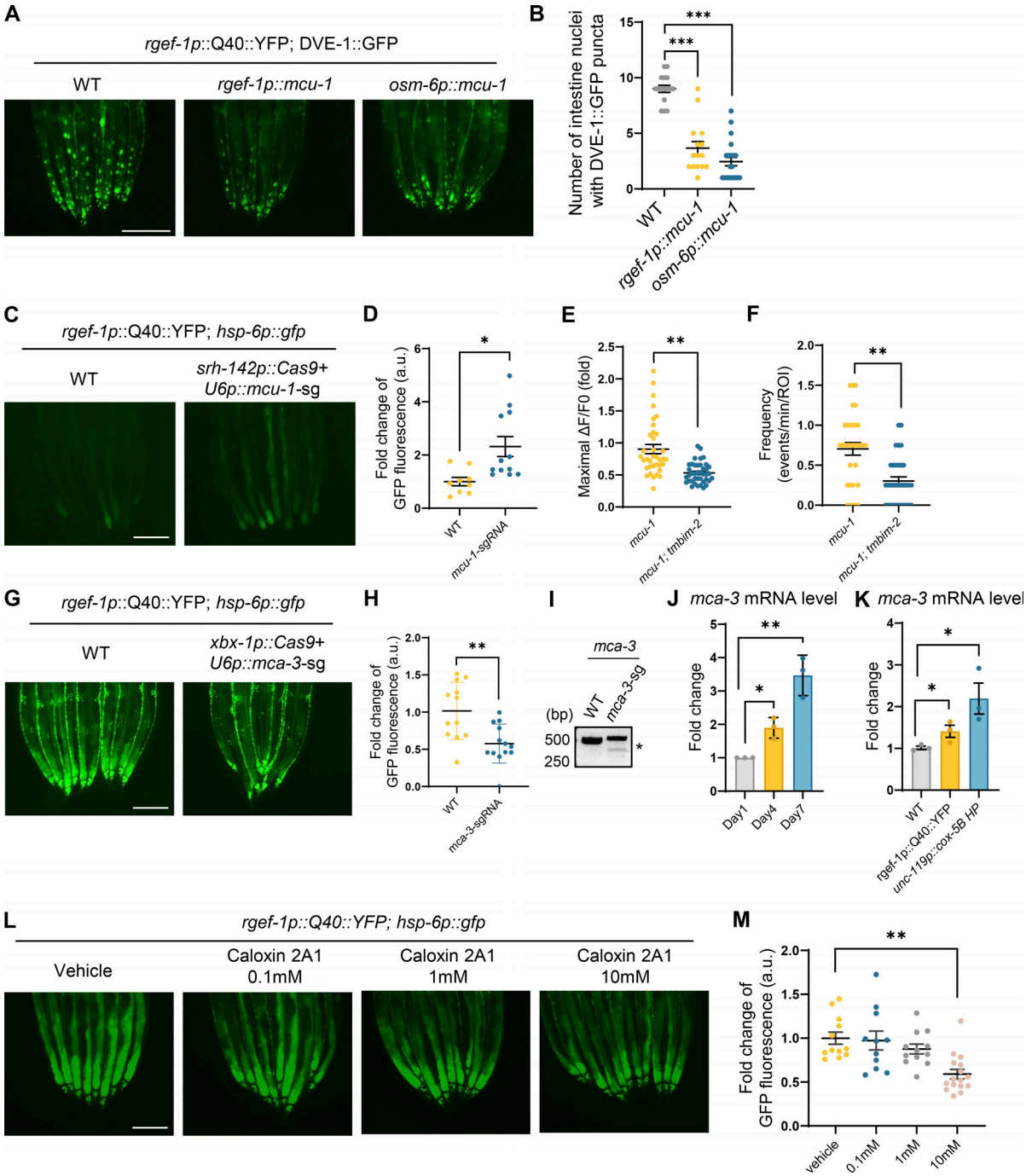

Figure S4. **Overexpression of MCU-1 and loss of *mca-3* in neurons partially suppresses neuronal-to-intestinal UPR^{mt} activation. (A)** Representative photomicrographs of *dve-1* reporter in WT; pan-neuron overexpressing MCU-1 *(rgef-1p::mcu-1)*; ciliated-sensory neuron overexpressing MCU-1 (*osm-6p::mcu-1*) animals with neuronal Q40::YFP, respectively. Scale bar, 250 µm. **(B)** Quantification of *dve-1p::dve-1::gfp* expression in the entire intestine of animals as depicted in A. *n* ≥ 15 worms. **(C)** Representative photomicrographs of *hsp-6* reporter in WT and ADF neuron *mcu-1* knockdown animals (*srh-142p::Cas9+u6p::mcu-1 sgRNA*) with neuronal Q40::YFP, respectively. Scale bar, 250 µm. **(D)** Quantification of *hsp-6p::gfp* expression in the entire intestine of animals as depicted in C. *n* ≥ 15 worms. **(E)** Quantification of PM-GCaMP6 maximal fluorescence intensity changes in WT and *tmbim-2; mcu-1(ju1154)* animals. *n* ≥ 20 worms. **(F)** Quantification of the frequency with GCaMP6f fluorescence intensity changes in WT and *tmbim-2; mcu-1(ju1154)* animals. *n* ≥ 20 worms. **(G)** Representative photomicrographs of *hsp-6* reporter in ciliated neuronal knockout of *mca-3* with neuronal Q40::YFP worms. Scale bar, 250 µm. **(H)** Quantification of *hsp-6p::gfp* expression in the entire intestine of animals as depicted in G. *n* ≥ 15 worms. **(I)** Representative DNA gels of T7E1 assay identifying the PCR products amplified from genomic DNA of control worms or worms with *mca-3* deletion in ciliated sensory neurons. **(J)** Quantification of *mca-3* mRNA levels in day1 (grey), day4 (yellow) and day7 (blue) WT adult animals. *n* ≥ 3 biologically independent samples. **(K)** Quantification of *mca-3* mRNA levels in WT (grey), neuronal overexpressing Q40 (yellow) and neuronal *cox-5B* knockdown (blue) animals. *n* ≥ 3 biologically independent samples. **(L)** Representative photomicrographs of *hsp-6* reporter in neuronal Q40::YFP animals with PMCA inhibitor Caloxin 2A1, respectively. Scale bar, 250 µm. **(M)** Quantification of *hsp-6p::gfp* expression in the entire intestine of animals as depicted in L. *n* ≥ 10 worms. ***P < 0.001; **P < 0.01; *P < 0.05 via unpaired two-tailed Student's *t* test. Error bars, SEM. Source data are available for this figure: SourceData FS4.

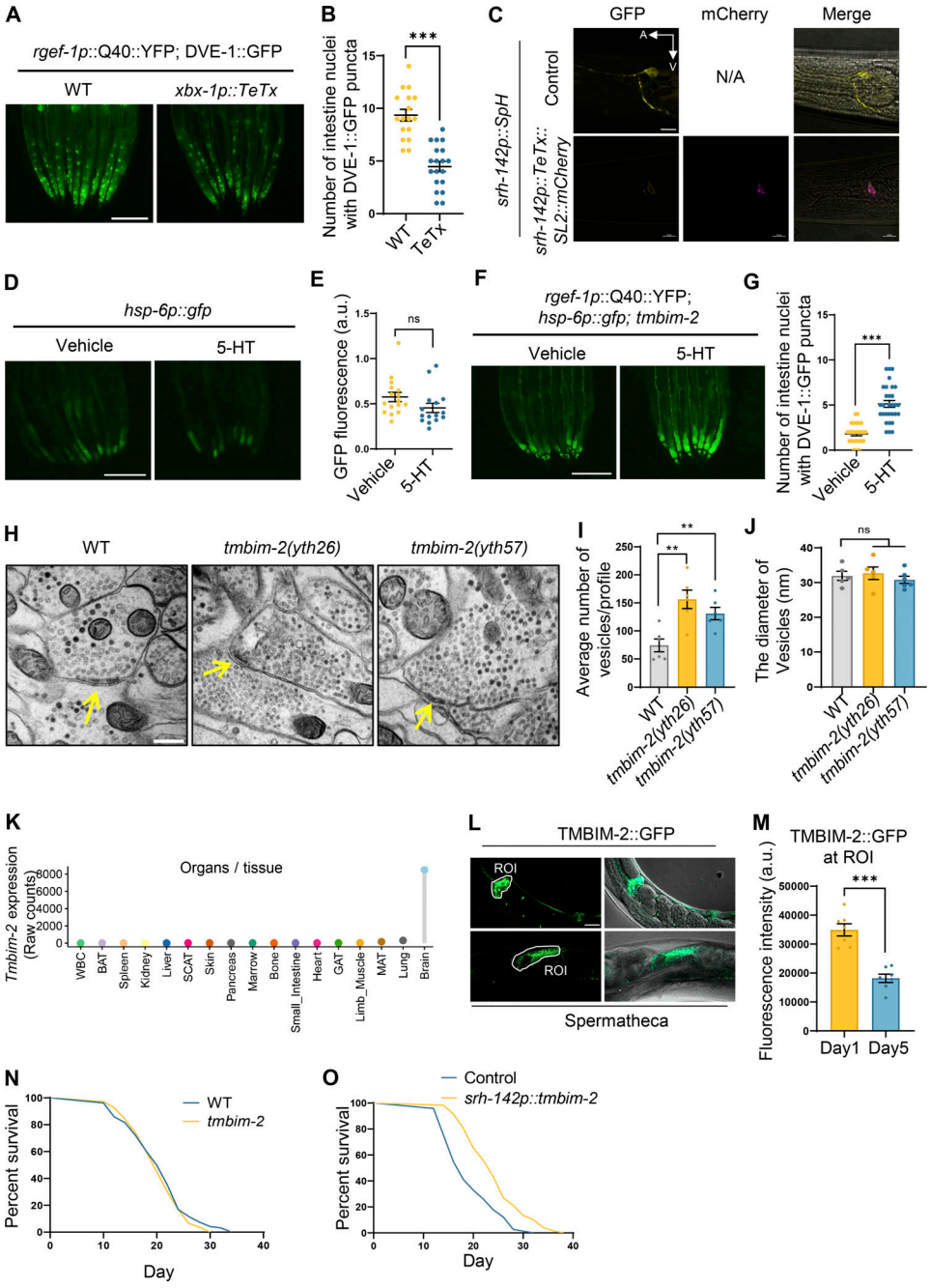

Figure S5. **Supplementation of serotonin restored the systemic UPR^{mt} activation in *tmbim-2* mutants. (A)** Representative photomicrographs of *dve-1* reporter in animals expressing neuronal Q40 and neurotoxin TeTx in ciliated sensory neurons (*ythEx488[xbx-1p::TeTx::sl2::mcherry]*). Scale bar, 250 µm. **(B)** Quantification of the number of intestinal nuclei puncta with GFP signal per worm as shown in A. $n \geq 15$ worms. **(C)** Representative photomicrographs of the ADF neurotransmitter exocytosis reporter (ythEX766[srh-142p-SYP-Phluorin+unc-119(+)]) in control and srh-142p::TeTx::SL2::mCherry expressing animals. For the control group, mCherry channel image was not acquired (N/A) due to the absence of mCherry expression. The imaging used Z-stacks. Scale bar, 10 µm. **(D)** Representative photomicrographs of *hsp-6* reporter (*zcIs3[hsp-6p::gfp]*) expression in animals treated with vehicle control or 50 mM serotonin (5-HT). **(E)** Quantification of *hsp-6p::gfp* expression. The genotypes are as in D. $n \geq 15$ worms. **(F)** Representative photomicrographs of *hsp-6* reporter expression in *rgef-1p::Q40::yfp*; *tmbim-2(yth26)* animals treated with vehicle control or 50 mM 5-HT. **(G)** Quantification of *hsp-6p::gfp* expression. The genotypes are as in F. $n \geq 15$ worms. **(H)** Representative TEM images of synaptic profiles, including WT, *tmbim-2(yth57)*, and *tmbim-2(yth26)*. Arrows indicate active zone; Scale bar, 200 nm. **(I)** Quantification of the number of synaptic vesicles at the active zone as shown in H. $n \geq 5$ worms. **(J)** Quantification of the size of synaptic vesicles at the active zone as shown in H. $n \geq 5$ worms. **(K)** Dot plot shows the average expression of *Tmbim2* in 17 mouse organs or tissue at the age of 3 mo. WBC, white blood cells; BAT, brown adipose tissue; SCAT, subcutaneous adipose tissue; GAT, gonadal adipose tissue; MAT, mesenteric adipose tissue. **(L)** Representative confocal photomicrograph of animals spermatheca expressing TMBIM-2 at different ages. The imaging used z-planes. Scale bar, 20 µm. **(M)** Quantitative analysis of TMBIM-2::GFP protein levels in ROI shown in L. $n \geq 8$ worms. **(N)** Survival analysis of WT (blue) and *tmbim-2 (yth26)* (yellow); $n \geq 80$ worms. **(O)** Survival analysis of control (blue) and ADF neuron overexpressing TMBIM-2 (yellow); $n \geq 80$ worms. ***P < 0.001, **P < 0.01, ns denotes P > 0.05 via unpaired two-tailed Student's *t* test. In N and O, we used The Log-rank (Mantel-Cox) test for statistical analysis. Error bars, SEM.

Video 1. **Neuronal mitochondrial perturbation triggers plasma-membrane Ca^{2+} oscillations within synapse of ADF neurons in a TMBIM-2-dependent manner.** Representative fluorescence intensity images of PM-GCaMP6f (yellow) expressed ADF presynaptic vesicle marker (magenta) with WT; neuronal *cox-5B* knockdown; *tmbim-2(yth130)*; neuronal *cox-5B* knockdown+*tmbim-2(yth130)* background, respectively. The PM-GCaMP6f fluorescence signal detected by confocal LSM980 with Airyscan 2 @10 Hz Multiplex SR-4Y Modes, related to Fig. 3, B–E. The GCaMP6f signal was imaged for 60 s. Scale bar: 2 µm. The video was recorded at 10 frames per second (fps). The playback speed is set to real-time, meaning that the video reflects the actual temporal dynamics of the Ca^{2+} oscillations observed in the experiment.

Provided online are Table S1, Table S2, Table S3, and Table S4. Table S1 contains information on *C. elegans* strains. Table S2 shows the list of primers in this study. Table S3 shows the lifespan date in this study. Table S4 shows the list of genes identified in the IP-MS experiments.